ABSTRACT

Title of Document: TELLURIUM/POROUS CARBON COMPOSITE CATHODE FOR LI-ION BATTERIES AND CARBON NANOFIBERS ANODE FOR NA/K-ION BATTERIES

Ying Liu, Master of Science, 2014

Directed By: Professor, Chunsheng Wang, Chemical and Biomolecular Engineering
Professor, David Bigio, Mechanical Engineering

Carbon materials are often used to enhance the electronic conductivity in anodes or cathodes of Li-ion batteries (LIBs), as well as to support other active materials in high-capacity nanocomposite electrodes. A novel lithium-tellurium battery was established here using tellurium/porous carbon composite (Te/C), which was synthesized by a vacuum-liquid-infusion method. Owing to the physical confinement of Te by porous carbon matrix, the Te/C electrode is capable to deliver a high reversible volumetric capacity of 1400 mAh/cm$^3$ for up to 1000 cycles and exhibits a good rate capability. In addition, *in situ* study of the electrochemically-driven sodiation and potassiation of individual bilayer carbon nanofibers (CNFs) by transmission electron microscopy (TEM) was also conducted to investigate the application of carbon based materials in sodium-ion batteries (NIBs) and potassium-ion batteries (KIBs), which indicates that disordered carbon possesses great potential for sodium and potassium storage.

# TELLURIUM/POROUS CARBON COMPOSITE CATHODE FOR LI-ION BATTERIES AND CARBON NANOFIBERS ANODE FOR NA/K-ION BATTERIES

By

Ying Liu

Thesis submitted to the Faculty of the Graduate School of the
University of Maryland, College Park, in partial fulfillment
of the requirements for the degree of
[Master of Science]
[2014]

Advisory Committee:
Professor Chunsheng Wang, Chair
Professor David Bigio
Professor Nam Sun Wang
Professor Dongxia Liu

# Dedication

To my family:

Thank you for your unconditional love and support. Thank you for your unwavering faith and absolute belief in my abilities.

# Acknowledgements

It is important to take this opportunity to express my sincere gratitude to all of those who have helped me during my period of study. First and foremost, I would like to thank my advisor, Dr. Chunsheng Wang, and my co-advisor, Dr. David Bigio. I am really honored to work under their guidance.

Next, I would like to thank Dr. Nam Sun Wang and Dr. Dongxia Liu for serving on my committee and taking time attending my thesis defense for master's degree.

I would like to thank all the members in Dr. Chunsheng Wang's research group, especially Dr. Yujie Zhu and Dr. Yunhua Xu for helping me during my research years in the group.

Finally, I would like to thank my family for all the support they have given to me throughout my time in Maryland.

# Table of Contents

# List of Tables

# List of Figures

second, fifth and twentieth cycle in a coin cell for Na-ion battery. The electrodes are tested in the voltage range of 0-1.2 V (vs $Na^+/Na$) at a current density of 50 mA/g, with the electrolyte of 1 M $NaPF_6$ dissolved in the mixture of EC+DMC (1:1 by volume). The specific capacity is calculated based on the mass of *d*-C, which is about 75% of the total mass of CNFs.

**Figure 3.4** Charge-discharge curves for bilayer CNF electrodes in the second, third and fifth cycle in a coin cell for K-ion battery. The electrodes are tested in the voltage range of 0-1.2 V (vs $K^+/K$) at a current density of 50 mA/g, with the electrolyte of 1 M $KPF_6$ dissolved in the mixture of EC+DMC (1:1 by volume). The specific capacity is calculated based on the mass of *d*-C, which is about 75% of the total mass of CNFs.

**Figure 3.5** Cycling stability and Coulombic efficiency measured for bilayer CNF electrodes in a coin cell for Na-ion battery.

**Figure 3.6** Cycling stability and Coulombic efficiency measured for bilayer CNF electrodes in a coin cell for K-ion battery.

**Figure 3.7** Geometry and structure changes of a bilayer CNF during sodiation under a beam-blank condition. (a, c) Pristine CNF. (b, d) Sodiated CNF.

**Figure 3.8** The line scan profiles of C and Na across the CNF after sodiation. The green arrows point to the peak positions of Na and C intensity profiles.

**Figure 3.9** Electron diffraction patterns (EDPs) of the CNF (a) before and (b) after sodiation. The average spacing of {0002} planes is about 3.38 Å in the pristine CNF. Two sets of patterns form after sodiation; the average spacing of {0002} planes in *c*-C and *d*-C increases to 3.67 Å and 4.16 Å, respectively.

**Figure 3.10** Microstructure evolution of a bilayer CNF during potassiation. The

experiment was conducted under beam-blank. (a-b) Morphologies of pristine and potassiated CNFs. A crack forms after full potassiation, as indicated by the red arrow in (b). (c-d) EDPs of the CNF before and after potassiation. For the pristine CNF, the average spacing of {0002} planes is about 3.39 Å. The EDP splits into two sets of patterns with different lattice spacings after potassiation. The average spacing of {0002} planes for *c*-C increases to 3.69 Å after full potassiation, while the one for *d*-C increases to ~ 4.18 Å.

**Figure 3.11** Sodiation-induced crack nucleation and propagation in a hollow bilayer CNF under a beam-on condition with very weak electron-beam exposure. (a) Pristine CNF. (b-g) The dynamic process of the sodiation-induced crack nucleation and propagation. The red arrows indicate the crack and its propagation front.

**Figure 3.12** Sodiation-induced cracks in a bilayer CNF under beam-on with very weak electron-beam exposure. (a) Pristine CNF. (b) Sodiated CNF with cracks formed. (c-d) Zoom-in images showing the cracks. (e-f) EDPs of the CNF before and after sodiation.

**Figure 3.13** Additional examples of crack formation in bilayer CNFs after sodiation. The experiments were conducted under beam-blank. The red arrows point to the cracks.

**Figure 3.14** EDPs of the CNF before and after the sodiation under beam on condition.

**Figure 3.15** Zoom-in images showing the cracks close to the *c*-C/*d*-C interface of CNF after sodiation under beam on condition.

**Figure 3.16** Microstructure evolution of monolithic *d*-C CNFs with solid (a) or hollow (b) structures. No cracking is observed during the sodiation of these

monolithic *d*-C CNFs. EDP confirms that the CNFs are sodiated.

**Figure 3.17** Schematic of crack formation at the *c*-C/*d*-C interface, which is caused by a large radial tensile stress $\sigma_r$ at the interface.

**Figure 3.18** Normalized radial stress ($\sigma_r / E$) versus radial distance *r*, being zero at the inner wall of the bilayer tube. The blue line corresponds to $\varepsilon_r^{c,d-C} = 0.12,\ \varepsilon_\theta^{c,d-C} = \varepsilon_z^{c,d-C} = 0.029$ , while the green line corresponds to $\varepsilon_r^{c,d-C} = 0.11,\ \varepsilon_\theta^{c,d-C} = \varepsilon_z^{c,d-C} = 0.034$.

**Figure 3.19** (a, d) A pristine CNF with *a*-Si coating (~19 nm in thickness). The diameter of the inner wall is about 80 nm. (b) Upon sodiation, the diameter of the inner wall decrease to ~ 62 nm at the moment of crack formation. (c, e) The crack finally forms along the longitudinal direction of the *a*-Si/CNF system. The thickness of the *a*-Si coating does not change after sodiation, indicating no reaction occurs. (f-g) EDPs of the pristine and sodiated *a*-Si/CNF. The sodiated CNF exhibits a typical split EDP, while no change is observed in the diffraction rings of *a*-Si before and after sodiation, confirming no reaction occurs in *a*-Si.

**Figure 3.20** Microstructure evolution of an amorphous silicon-coated CNF (*a*-Si/CNF) before and after sodiation. (a-d) Sequential images showing the crack nucleation and growth upon sodiation, accompanied with the decrease of the inner tube diameter. (e-f) Zoom-in images showing the cracks the interface between *c*-C and *d*-C. The thickness of the surface *a*-Si layer does not change after sodiation, indicating no reaction occurring.

# Chapter 1: Introduction

## *1.1 Background*

The large-scale storage of electrical energy for applications in electrical grids requires battery systems with high energy/power density, superior cycling and reliability stability, as well as low cost[1,2]. During the past decade, great effort has been devoted to Li-ion batteries (LIBs), and significant progress has been realized in the development of high capacity electrodes for LIBs. Since significant progress has been realized in the development of new anodes with high performance, such as silicon, tin, metal sulfides and metal oxides based materials[3-9], the energy/power density of current LIBs is mainly hindered by the cathode side, thus exploring and developing new high-energy density cathodes materials is of great importance for the future success of lithium-ion battery.

In addition, due to the limited energy density and high cost of LIBs, batteries based on other alkali-metals, such as Na-ion batteries (NIBs) and K-ion batteries (KIBs)[10-12], have attracted great attention, owing to their comparatively high natural abundance and low cost [10,12-14]. Considering the similar chemical properties of Li, Na and K, the anode and cathode materials used in LIBs are being investigated for their applications in NIBs and KIBs in the past few years. Carbonaceous materials have great potential for applications as anodes for NIB and KIBs. However, the application of the carbon-based anodes in NIBs and KIBs remains largely unexplored, compared with their LIB counterparts. Therefore, it is essential to understanding the electrochemical reactions and associated structure-property relationships of carbon-

based anodes during sodiation and potassiation, thereby paving the way for future development of the novel carbon-based or carbon-supported nanocomposite anodes for NIBs and KIBs.

*1.2 Cathode materials for Lithium-ion batteries*

During the past decade, great efforts have been put on alternative anode materials with high theoretical capacity, excellent ratability and long cycle life. And a lot of progress has been made on the insertion alloys (Si, Sn, Ge), redox metal oxides ($Fe_2O_3$ and CuO etc.) and carbon (soft carbon and hard carbon), which have been considered as promising anode materials for the next-generation lithium-ion batteries[15-20]. Unlike the anode side, the comparatively low storage capacity of the most known cathode materials has been recognized as a major limiting factor in the overall performance of Li-ion batteries, thus exploring and developing new high-energy density cathodes materials is of great importance for the future success of lithium-ion battery.

Except state-of-art transition metal oxide cathode for LIBs, sulfur has been extensively studied as a cathode material for Li-S batteries, because of their low cost and high theoretical gravimetric energy density (2570 Wh/kg)[21]. However, sulfur cathodes are challenged by three major issues:[22-24] the low electronic conductivity of S and formed $Li_2S$, the large volume expansion after lithiation (~80%), and "shuttle effect" caused by the dissolution of high order polysulfide intermediates into electrolyte and subsequent migration and reaction with Li anode. Therefore, current Li-S batteries suffer from low Coulombic efficiency and rapid capacity decay,

blocking the commercialization of S cathode in battery industries. Over the years, great efforts have been devoted to address these problems and many strategies have been proposed, such as impregnating sulfur into the porous carbon[25, 26], encapsulating sulfur with graphene oxide[24] or conductive polymers[27, 28], entrapping sulfur into the yolk-shell structure[23], or reducing the solubility of polysulfides by alternative electrolyte or additives [29].

Recently, it has been reported that selenium (Se), the element in chalcogens family (sulfur, selenium, tellurium), can also be treated as a perspective candidate for cathode material[30-32]. With similar chemical properties but higher electronic conductivity, lithium-selenium (Li-Se) batteries can deliver a reversible gravimetric capacity of 675 mAh/g theoretically. However, the electronic conductivity is still not high enough. Thus, inspired by this, tellurium, another element in the chalcogens family, which possess the highest electronic conductivity among all non-metallic materials endows it further advantages compared with sulfur and selenium. Despite the gravimetric capacity of tellurium electrode ($Li_2Te$: 419 mAh/g) is lower than that of selenium ($Li_2Se$:675 mAh/g) and sulfur ($Li_2S$:1672 mAh/g), the higher density provides it a high volumetric capacity. In fact, the battery packing space is usually limited in portable devices, such as EV and HEV, thus volumetric capacity is actually more important than gravimetric capacity[31,33]. Therefore, the superior electronic conductivity as well as high volumetric capacity makes tellurium a potential candidate for electrode material in lithium-ion batteries.

### *1.3 Anode materials for Sodium-ion batteries and Potassium-ion batteries*

The potential anode materials for NIBs and KIBs include carbonaceous

materials, Sn, Sb, and metal oxides[10,13-14,34-38]. Among these candidates, however, carbonaceous materials[11,39-45] are most promising, given their successful applications in commercial LIBs and particularly low cost, natural abundance, small volumetric expansion during alloying with alkali-metals, in contrast to other anode materials such as Sn[36].

Graphite has been used as the anode of current commercial LIBs with a theoretical capacity of 372 mAh/g[46]. However, only a small amount of Na ions can be stored in the graphite anode of NIBs. Such a limitation has been often attributed to the higher intercalation energy barrier of Na ions[10,11,47]. So far, the highest capacity for carbonaceous anodes reported in NIBs is about 300 mAh/g in hard carbon, whose usage is severely limited by its poor cyclability[45].

Recently, the disordered or amorphous carbon materials were found to exhibit much improved cyclability[11,41,48]. For example, the disordered hollow carbon nanowires showed a reversible capacity as high as 251 mAh/g with 82.2% capacity retention after almost 400 sodiation-desodiation cycles[41], which is much better than hard carbon[42,45]. Moreover, carbon is often used to enhance electron conduction in anodes or cathodes of LIBs and NIBs, as well as to support other active materials in high-capacity nanocomposite anodes for LIBs and NIBs[49-55]. However, the application of the carbon-based anodes in KIBs remains unknown. Therefore, it is essential to understanding the electrochemical reactions and associated structure-property relationships of carbon-based anodes during sodiation and potassiation.

### *1.4 In situ TEM technology for batteries*

In order to understand the microscopic mechanism of electrochemical reaction

and electrode degradation during charge/discharge process of LIBs, a novel nanobattery inside a transmission electron microscope (TEM) was created by Liu *et al*[56], which makes real time and atomic scale observations of lithiation/delithiation processes possible. The nanobattery cells have two types, one based on room temperature ionic liquid electrolytes, which consists of a single nanowire anode, an ionic liquid electrolytes and a bulk $LiCoO_2$ cathode, and the other one based on all solid components, which uses $Li_2O$ as a solid electrolyte and metal Li as the anode.

By using this unique technique, a direct study of the morphology and microstructure changes of individual nanowires and nanoparticles during electrochemical lithiation and delithiation can be studied in a real time at high tempo-spatial resolutions. And this nanobattery setup has been successfully employed in the study of reaction kinetics and degradation mechanism of $SnO_2$ nanowires, Si nanowires, Sn nanoparticles, carbon nanotubes, carbon nanofibers, graphene nanoribbons, Ge nanowires, FePO4 microparticles etc. during electrochemical lithiation/sodiation for LIBs and NIBs[56]. And their results provide important clues for the structure evolution and failure mechanism of electrode materials during charge/discharge process for batteries, shedding the light on the fundamental science to improve the battery design.

### *1.5 Objective of this research*

The objective of the current research is to make a significant contribution to the advancement of cathode for lithium-ion batteries, and anode for sodium-ion batteries and potassium-ion batteries.

Specifically, the two main goals of this study are: (1) Synthesis and characterize of Te/porous carbon composite cathode; study the electrochemical behavior of Te/C cathode through charge/discharge curve, cycling stability and ratability. (2) Study the electrochemical behavior carbon nanofibers (CNFs) in Na-ion batteries and K-ion batteries; investigate the microstructure evolution of CNFs during Na and K insertions in real time by using a nanoscale battery setup inside a transmission electron microscope (TEM);

The subsequent three chapters discuss the efforts to achieve the stated goals. Chapter 2 describes the tellurium/porous carbon composite cathode for Li-ion batteries. Chapter 3 focuses on the *in situ* TEM study of electrochemical sodiation and potassiation of carbon nanofibers. Chapter 4 includes the conclusion of this thesis paper and the discussion of future work.

# Chapter 2: Tellurium/porous carbon composite cathode for Li-ion batteries

Ying Liu, Jiangwei Wang, Yujie, Zhu, Yunhua Xu, David Bigio and Chunsheng Wang, *J. Mater. Chem. A*, **2014**, DOI: 10.1039/C4TA02075H

## *2.1 Introduction*

During the last two decades, rechargeable lithium-ion batteries (LIBs) have been wildly used as the power sources for various mobile electronics, including cellular phones, laptop computers and digital cameras[1,2,57]. In recent years, the rapid development of electric vehicles (EVs), hybrid electric vehicles (HEVs) and large-scale renewable energy storage calls for secondary batteries with high energy/power density, superior cycling and reliability stability, as well as low cost[58-60]. Recently, significant progress has been realized in the development of high capacity electrodes for LIBs. The materials based on elements in period 5 (In, Sn, Sb) have been demonstrated as promising anodes to replace commercial graphite anodes in Li-ion batteries due to their high capacity, while materials based on elements in group 16 (S and Se) have been well identified as the next generation cathodes due to almost 10 times higher capacity than current metal oxide cathodes[61-67]. However, the lithiation/delithiation behavior of electrodes based on element tellurium (Te), the element crossing the period 5 and group 16, has not been studied yet.

Owning to a large volume change of these high capacity electrodes, these materials will be cracked or even pulverized into small powders after periodical lithiation/delithiation process, thus resulting in rapid capacity decline and batteries

failure. Carbon materials are often used to enhance the electronic conductivity in anodes or cathodes of Li-ion batteries, as well as to support other active materials in high-capacity composite electrodes. Thus, the most effective method is to disperse these active materials into a porous carbon matrix to support and mechanically confine these cracked materials, with the purpose of improving the cycling stability of electrode.

In chalcogens group, element sulfur has been extensively studied as a cathode material for Li-S batteries, because of their low cost and high theoretical gravimetric energy density (2570 Wh/kg)[21]. However, sulfur cathodes are normally challenged by three major issues:[22-24] First, the electronic conductivity of S and formed $Li_2S$ are very low, resulting in a poor rate capability and low utilization of active materials. Second, the large volume expansion after lithiation (~80%) brings to particle pulverization and structure reorganization. Third, the dissolution of high order polysulfide intermediates into electrolyte and subsequent migration and reaction with Li anode leads to the transport of low-order polysulfides back to the cathode side, resulting in "shuttle effect". Therefore, current Li-S batteries suffer from low Coulombic efficiency and rapid capacity decay, blocking the commercialization of S cathode in battery industries. Over the years, great efforts have been devoted to address these problems and many strategies have been proposed, such as impregnating sulfur into the porous carbon[25,26], encapsulating sulfur with graphene oxide[24] or conductive polymers[27,28], entrapping sulfur into the yolk-shell structure[23], or reducing the solubility of polysulfides by alternative electrolyte or additives[29].

Recently, it has been reported that selenium (Se), the element in chalcogens

family (sulfur, selenium, tellurium), can also be treated as a perspective candidate for cathode material[30-32]. With similar chemical properties but higher electronic conductivity (Se: $1 \times 10^{-4}$ S/m, S: $5 \times 10^{-16}$ S/m), lithium-selenium (Li-Se) batteries can deliver a reversible gravimetric capacity of 675 mAh/g theoretically. However, although Se exhibits promising advantages compared with S, the electronic conductivity is still not high enough. Thus, inspired by this, tellurium, another element in the chalcogens family, which possess the highest electronic conductivity among all non-metallic materials ($2 \times 10^{2}$ S/m), endows it further advantages compared with sulfur and selenium, such as high utilization rate and better kinetics during charge/discharge process. Despite the gravimetric capacity of tellurium electrode ($Li_2Te$: 419 mAh/g) is lower than that of selenium ($Li_2Se$:675 mAh/g) and sulfur ($Li_2S$:1672 mAh/g), the higher density provides it a high volumetric capacity (2621 mAh/cm$^3$ based on density of 6.24 g/cm$^3$), which is comparable to that of selenium (3253 mAh/cm$^3$ based on density of 4.82 g/cm$^3$) and sulfur (3467 mAh/cm$^3$ based on density of 2.07 g/cm$^3$). In fact, the battery packing space is usually limited in portable devices, such as EV and HEV, thus volumetric capacity is actually more important than gravimetric capacity[31,33]. Therefore, the superior electronic conductivity as well as high volumetric capacity makes tellurium a potential candidate for electrode material in lithium-ion batteries.

In this study, a novel Te/C composite was synthesized by encapsulated liquid tellurium into the host of porous carbon at a high temperature of 600 $^{o}$C under vacuum environment. For the first time, the lithiation/delithiation behavior of Te/C composite was investigated in 1 M $LiPF_6$ in a mixture of ethylene carbonate/diethyl

carbonate (EC/DEC, 1:1 by volume) electrolyte at room temperature. The as prepared Te/C electrode can deliver and maintain a reversible volumetric capacity of 1400 $mAh/cm^3$ (224 mAh/g) at a current rate of 50 mA/g with a Coulombic efficiency up to 99% for 1000 cycles. As the current density increases from 50 mA/g to 1000 mA/g, the capacity retained about 47%, and 35% after current density increases up to 2000 mA/g. The high volumetric capacity, long cycle life, excellent Coulombic efficiency and good rate capability of Li-Te battery demonstrates that tellurium is a perspective electrode material candidate for high-energy storage and large-scale applications.

*2.2 Synthesis of Tellurium/porous carbon composite electrode*

The Te/C composite was synthesized by impregnating liquid tellurium into the porous carbon matrix through a vacuum-liquid-infusion method. Typically, solid tellurium (Sigma Aldrich Inc., USA) and porous carbon (Advanced Chemical Supply Inc., USA) were mix with a ratio of 1:1 by weight and sealed in a glass tube under vacuum. Heat treatment at 600 $^oC$ for 24 h was conducted to melt the solid tellurium (melting point is 450 $^oC$ ) and infuse it into the porous carbon.

The as prepared Te/C composite was mixed with carbon black and sodium alginate binder to form slurry at the weight ratio of 70:15:15. The electrode was prepared by casting the slurry onto the aluminum foil using a doctor blade and then drying at room temperature overnight followed by heating at 100 $^oC$ in a vacuum oven by overnight. The same method was used to fabricate the pure tellurium and porous carbon electrodes for comparison. The thickness of the coating on Al is approximately 20 μm and the loading of electrode is about 1 mg $cm^{-2}$. The electrode

was cut into circular pieces with diameter of 1.2 cm for coin-cell testing. Li-ion batteries were assembled with lithium as the counter electrode, 1 M $LiPF_6$ in a mixture of ethylene carbonate/diethyl carbonate (EC/DEC, 1:1 by volume) as the electrolyte, and Celgard®3501 (Celgard, LLC Corp., USA) as the separator. Electrochemical performance was tested using an Arbin battery test station (BT2000, Arbin Instruments, USA). Capacity was calculated on the basis of the mass of Te. GITT measurements were carried out by applying a pulse constant current (50 mA/g) with duration of 0.25 h, followed by 6 h relaxation to reach an equilibrium potential. Cyclic voltammograms at a scan rate of 0.1 mV/s between 0.8 and 2.5 V were tested using Solartron 1260/1287 electrochemical interface (Solartron Metrology, UK).

*2.3 Characterization of Tellurium/porous carbon composite*

Scanning electron microscopy (SEM) images were taken using a Hitachi SU-70 analytical ultra-high resolution SEM (Japan). Transmission electron microscopy (TEM) images were taken by JEOL (Japan) 2100F field emission TEM. Thermogravimetric analysis (TGA) was carried out using a thermogravimetric analyzer (TA instruments, USA) with a heating rate of 10 $^{o}C\ min^{-1}$ in air. X-ray diffraction (XRD) pattern was recorded by Bruker Smart1000 (Bruker AXS Inc., USA) using CuKα radiation. BET specific surface area and pore size and pore volume were tested using $N_2$ absorption on Micromeritics ASAP 2020 (Micromeritics Instrument Corp., USA). Raman measurements were performed on a Horiba Jobin Yvon Labram Aramis using a 532 nm diode-pumped solid-state laser, attenuated to give ~900 μW power at the sample surface.

### 2.3.1 SEM

Figure 2.1a show the SEM images of Te/C composite, which exhibits a well-formed flake-like shape, with the size of the flake in micro-scale. As compared with the pure porous carbon, illustrated in the figure 2.1b, no morphology change is observed after tellurium is infused into the porous carbon host, implying that most of the tellurium has been filled inside the porous carbon, which has been confirmed by the high resolution TEM images of Te/C composite, see Figure 2.2a.

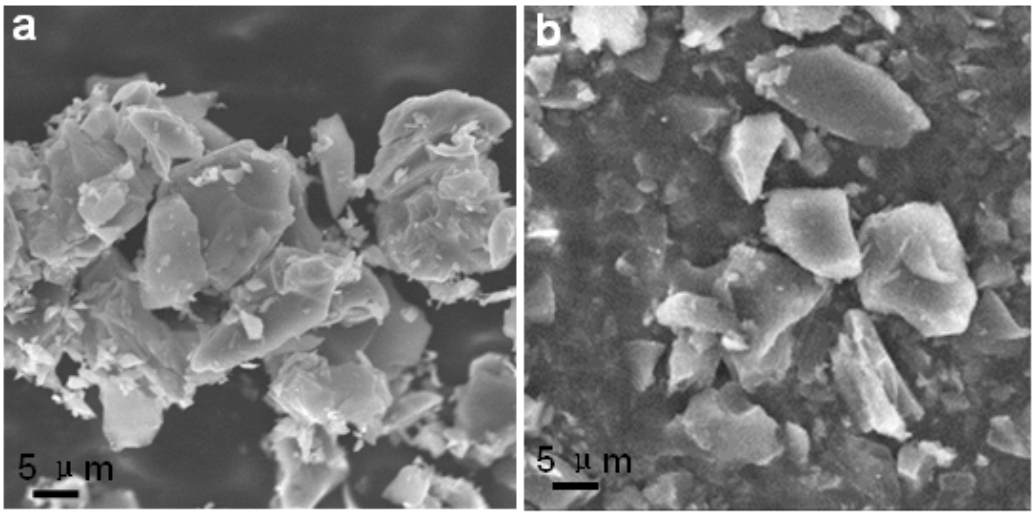


**Figure 2.1** (a) SEM images of the tellurium-impregnated porous carbon composite. (b) SEM images of the pure porous carbon.

### 2.3.2 TEM and EDS mapping profile

The TEM image in Figure 2.2a confirmed that the flake-like shape of Te/C composite, which is in good consistence with SEM results in Figure 2.1a and b. The high resolution TEM image in Figure 2.2b shows that tellurium has been filled into the porous carbon matrix. The elemental mapping images (Figure 2.2c, d and e) reveal that tellurium is homogeneously distributed in the porous carbon matrix and no

tellurium accumulation can be observed on the carbon surface, illustrating a perfect Te infiltration into porous carbon host. The uniform distribution and free of surface accumulation as well as excellent electronic conductivity of carbon and tellurium itself ensure a high utilization of active material and good kinetics during electrochemical reactions. The content of tellurium in Te/C composite is revealed to be 50 wt% by the TEM elemental analysis (Figure 2.3).

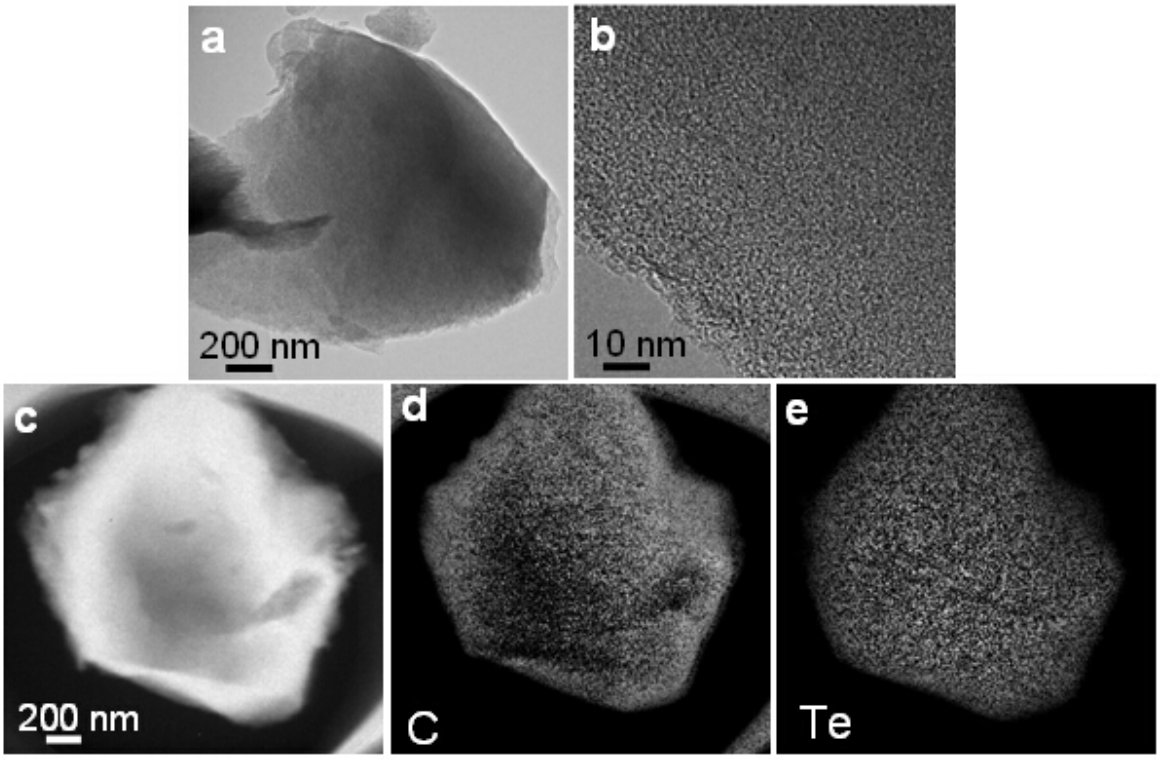


**Figure 2.2** (a) TEM image of Te/C composite. (b) High resolution TEM image of Te/C composite. (c) TEM and elemental mapping images of Te/C composite: (d) carbon and (e) tellurium.

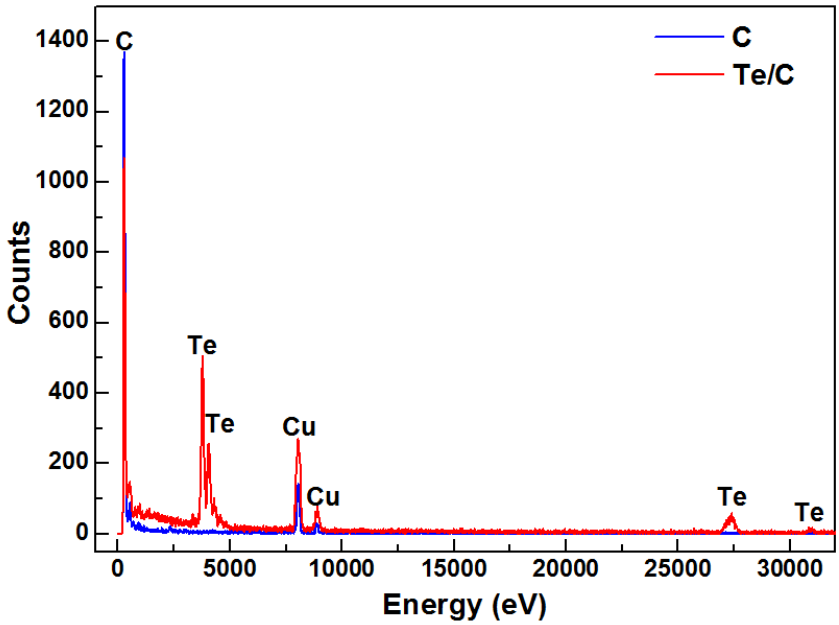


**Figure 2.3** TEM elemental analysis for Te/porous carbon composite.

### 2.3.3 TGA

The ratio of tellurium to carbon in Te/C composite can be further confirmed by the TGA measurement, and the result is shown in Figure 2.4. It can be seen that there is no weight loss observed from the room temperature to 350 $^{o}$C, indicating that the composite is stable up to 350 $^{o}$C in air, and no Te oxidation and carbon decomposition reactions occurred in the temperature range of 25-350 $^{o}$C. The weight loss from 350 to 480 $^{o}$C is the combination effects of weight loss from the carbon oxidation to carbon dioxide, $C + O_2 = CO_2$ and weight increase due to the oxidation of tellurium, $Te + O_2 = TeO_2$. The Te content can then be determined to be 50% using the following equation:

$$\text{Te (wt\%)} = \frac{\text{molecular weight of Te}}{\text{molecular weight of TeO}_2} \times \frac{\text{final weight of TeO}_2}{\text{initial weight of Te/C}} \times 100$$

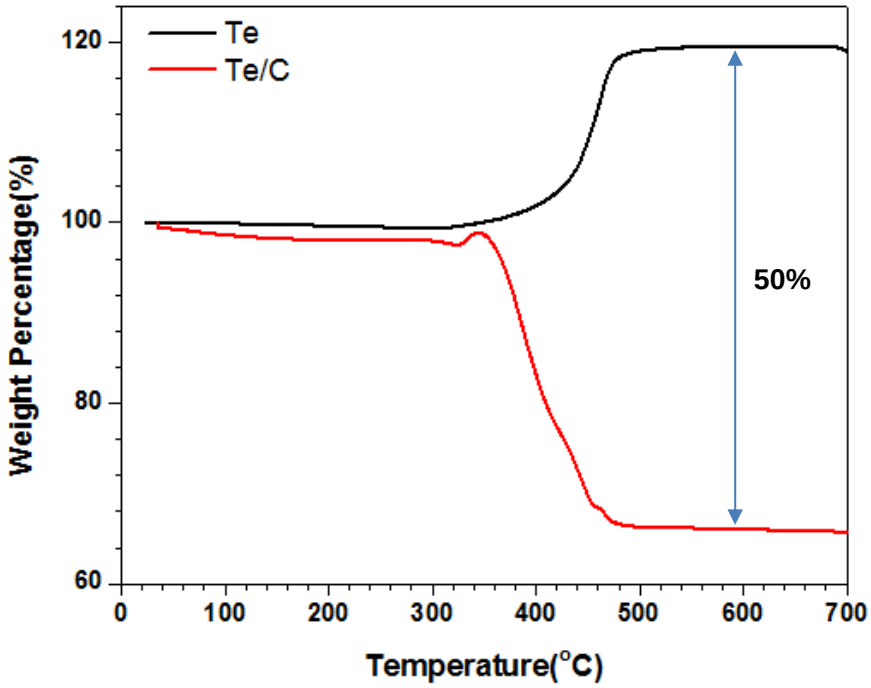


**Figure 2.4** TGA results of Te/C composite and pristine Te.

### 2.3.4 BET

The tellurium impregnation into porous carbon is also evidenced by the Brunauer–Emmett–Teller (BET) analysis, shown in Figure 2.5. The changes in porous structure of porous carbon before and after Te impregnation are summarized in Table 2.1. The specific surface area is calculated from the adsorption data in the relative pressure range of 0.05 to 0.3. Pore size distributions (PSDs) were determined from the adsorption branches of the isotherms using density functional theory (DFT). Total pore volumes were calculated from the amount of adsorption at a relative pressure, $P/P_0$, of 0.90. Micro-pore volumes were calculated using the *t*-plot method. The porous carbon has a large BET surface area of 1416 $m^2/g$ and high pore volume of 0.44 $cm^3/g$, with the average pore size about 2.5 nm. After infusion of tellurium, the BET surface area decreased dramatically to 353 $m^2/g$, and the pore volume

declined to 0.06 $cm^3/g$, indicating that most of the pores have been occupied by Te.

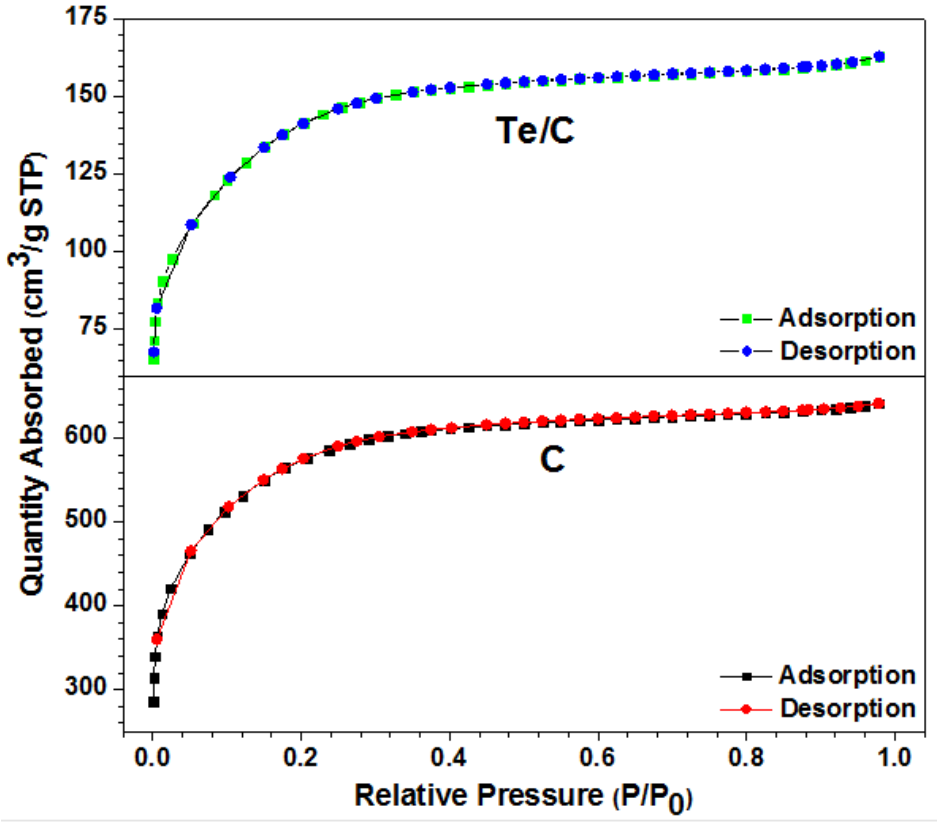


**Figure 2.5** BET Adsorption and desorption curve of the porous carbon and Te/C composite.

**Table 2.1** BET parameters of pure porous carbon and Te/C composite.

| Sample | BET Surface Area ($m^2/g$) | Pore Volume ($cm^3/g$) | Pore Size (nm) |
|---|---|---|---|
| C | 1416 | 0.44 | 2.3 |
| Te/C | 353 | 0.06 | 2.4 |

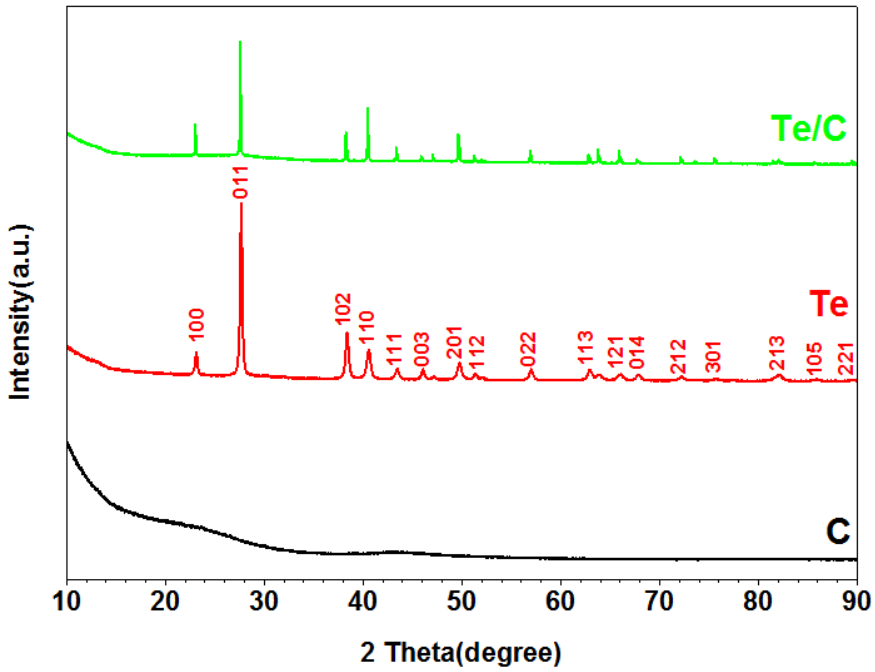


**Figure 2.6** XRD pattern of porous carbon, pristine Te and Te/C composite.

### 2.3.5 XRD

The infused tellurium in porous carbon exists in crystal structure as demonstrated by the XRD patterns of Te/C composite in Figure 2.6. For comparison, the XRD of both pristine Te and pure porous carbon are also shown in Figure 2.6. The porous carbon exhibits an XRD pattern for typical carbon materials. The Te/C composite displays well-defined diffraction pattern as the pristine tellurium (JCPDA File No. 79-0736), indicating that the infusion process did not change the crystal structure of tellurium.

### 2.3.6 Raman

The nature of tellurium in composite is further characterized using Raman spectroscopy. For comparison, porous carbon (C), pristine Te (Te), and manually mixed Te-C composite (Te&C) at the same ratio to the Te/C composite in room

temperature, are also analyzed using Raman spectroscopy, (Figure 2.7).

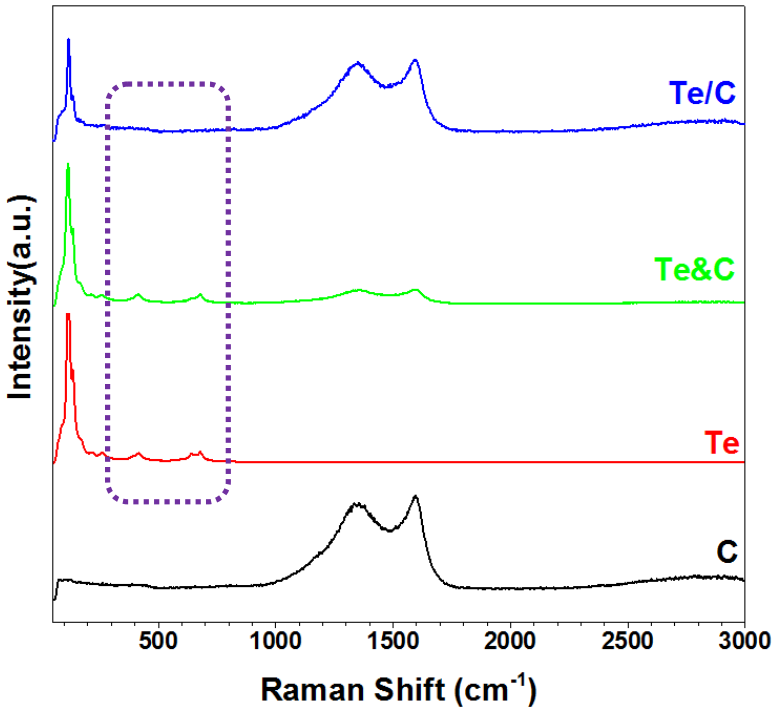


**Figure 2.7** Raman spectra of porous carbon, pristine Te, manually mixed Te&C, and Te/C composite.

For porous carbon, two broad peaks at 1350 $cm^{-1}$ and 1590 $cm^{-1}$ are attributed to the disordered (D) and graphitic (G) carbon, demonstrating that the porous carbon is partially graphitized. Typical Raman spectrum pattern of pristine tellurium is characterized by three peaks from 80 to 700 $cm^{-1}$, which are probably attributed to $E_2$ bond-bending, $A_1$ bonding-bending and $A_1$ bond-stretching modes of the crystalline trigonal tellurium, with a highly anisotropic crystal structure consisting of helical chains of covalently bound[68,69]. For Te/C composite, after infusing tellurium into porous carbon host, two small peaks from 400 to 700 $cm^{-1}$ disappear, although the

vibration peaks around 117 $cm^{-1}$ of Te remains,, implying the Te not only physically confined in porous carbon matrix, but also chemically bonds to carbon stabilizing tellurium in the supporting carbon matrix. The chemical bonding is probably induced by high temperature infusion process since the Te peak at 400 to 700 $cm^{-1}$ still exists in Te&C mixture prepared at room temperature (Figure 2c). The mixed Te&C exhibits a simple addition of tellurium and carbon Raman spectra separately, no any changes on the forms of Te itself. Therefore, the confinement of the porous carbon at high temperature remarkably altered the structure of tellurium.

*2.4 Electrochemical tests result and discussion*

Electrochemical performance of the Te/porous carbon composite cathodes were tested in coin cells (R2032) using the Li foil as a counter electrode, 1 M $LiPF_6$ solution in ethylene carbonate/diethyl carbonate (EC/DEC, 1:1 by vol. %) as electrolyte, and Celgard®3501 (Celgard, LLC Corp., USA) as the separator. The charge/discharge testing was carried out using an Arbin BT-2000 battery test station (BT2000, Arbin Instruments, USA) over the voltage range of 0.8-2.5 V versus $Li/Li^+$. All electrochemical experiments were conducted at room temperature and all capacity was calculated on the basis of the mass of Te. GITT measurements were carried out by applying a pulse constant current (50 mA/g) with duration of 0.25 h, followed by 6 h relaxation to reach an equilibrium potential. Cyclic voltammograms at a scan rate of 0.1 mV/s between 0.8 and 2.5 V were tested using Solartron 1260/1287 electrochemical interface (Solartron Metrology, UK).

a

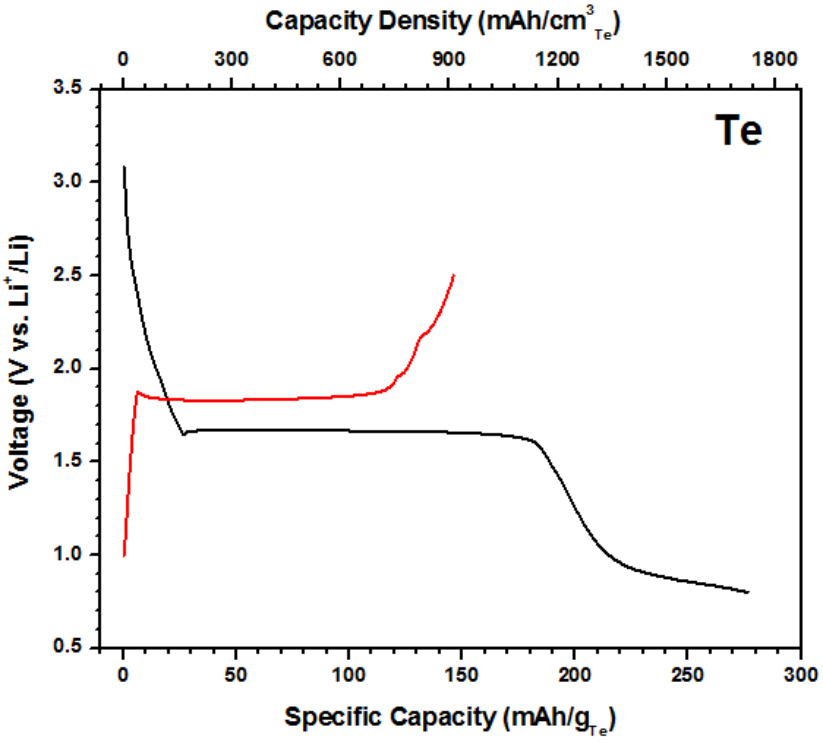
Capacity Density (mAh/cm$^3_{Te}$)
0
300
600
900
1200
1500
1800
Te
Voltage (V vs. Li$^+$/Li)
3.5
3.0
2.5
2.0
1.5
1.0
0.5
0
50
100
150
200
250
300
Specific Capacity (mAh/g$_{Te}$)

b

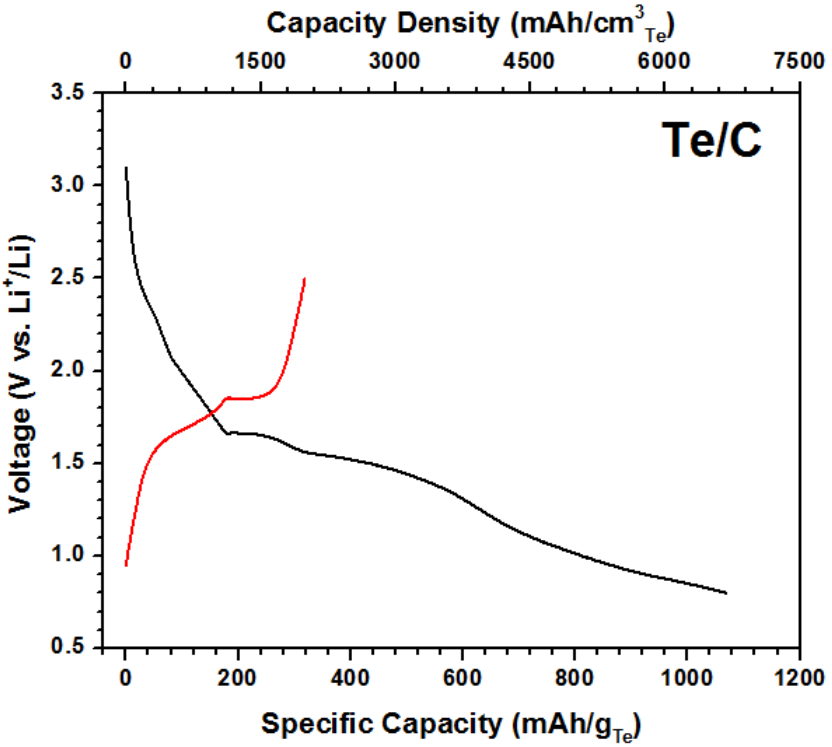
Capacity Density (mAh/cm$^3_{Te}$)
0
1500
3000
4500
6000
7500
Te/C
Voltage (V vs. Li$^+$/Li)
3.5
3.0
2.5
2.0
1.5
1.0
0.5
0
200
400
600
800
1000
1200
Specific Capacity (mAh/g$_{Te}$)

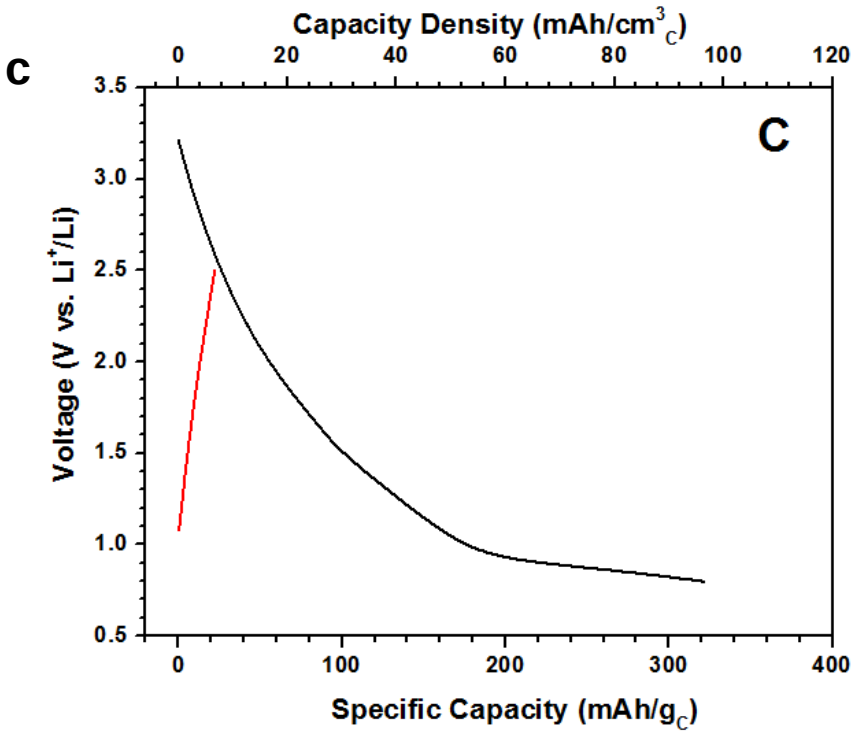


**Figure 2.8.** Charge/discharge profiles at the first cycle of (a) pristine Te electrode, (b) Te/C composite electrode and (c) porous carbon electrode in the electrolyte of 1 M $LiPF_6$ in a mixture of ethylene carbonate/diethyl carbonate (EC/DEC, 1:1 by volume) between 0.8-2.5 V at a current density of 50 mA/g.

### 2.4.1 Charge/discharge curve

The electrochemical performance of the Te/C composite was investigated in a coin cell using lithium metal as the counter and reference electrode, and 1 M $LiPF_6$ in a mixture of ethylene carbonate/diethyl carbonate (EC/DEC, 1:1 by volume) as electrolyte. All electrochemical experiments are conducted at room temperature, and all capacity is calculated based on the mass or volume of tellurium. Figure 2.8 shows the charge/discharge profiles of Te/C composite between 0.8-2.5 V at a current density of 50 mA/g, with the comparison of both pristine Te and porous carbon

electrodes at the same voltage range and current density.

As demonstrated in Figure 2.8a, pristine Te electrode displays a voltage plateau at 1.6 V in discharge and at 1.8 V in charge, with a discharge volumetric capacity of 1685 mAh/cm$^3$ (270 mAh/g) and charge volumetric capacity of 936 mAh/cm$^3$ (150 mAh/g) in the first cycle. The plateau at 0.9 V is attributed to porous carbon as demonstrated in Figure 2.8c. For Te/C composite (Figure 2.8b) , two slope-shaped voltage plateaus locating at 1.6 V and 1.4 V in discharge, 1.7 V and 1.9 V in charge process are observed. The extra voltage plateau at 1.4 V for discharge and 1.7 V for charge cannot be attributed to carbon since no voltage plateau above 1.0 V is observed in electrode made by pure porous carbon, see Figure 2.8c. The transition from well-defined single plateau of pure Te to two slope-shaped plateaus of Te/C is probably due to the interaction between Te and porous carbon, which is also observed in S/C and Se/C composites[24,26,27].

The interaction between Te and porous carbon was confirmed by Raman measurement in Figure 2.7. The Te/C composite delivers a volumetric capacity of 6739 mAh/cm$^3$ (1080 mAh/g) in first discharge and 1872 mAh/cm$^3$ (300 mAh/g) in first charge process. The large irreversible capacity formed in the first cycle is mainly attributed to the formation of solid electrolyte interphase (SEI) film on the surface of the porous carbon[32], which is confirmed by the high irreversible capacity of porous carbon itself in Figure 2.8c. Since the porous carbon only provides 6 mAh/cm$^3$ volumetric capacity (20 mAh/g) (Figure 2.8c), the contribution from carbon to the total capacity of Te/C is negligible, therefore the capacity can be calculated based on the mass of tellurium only.

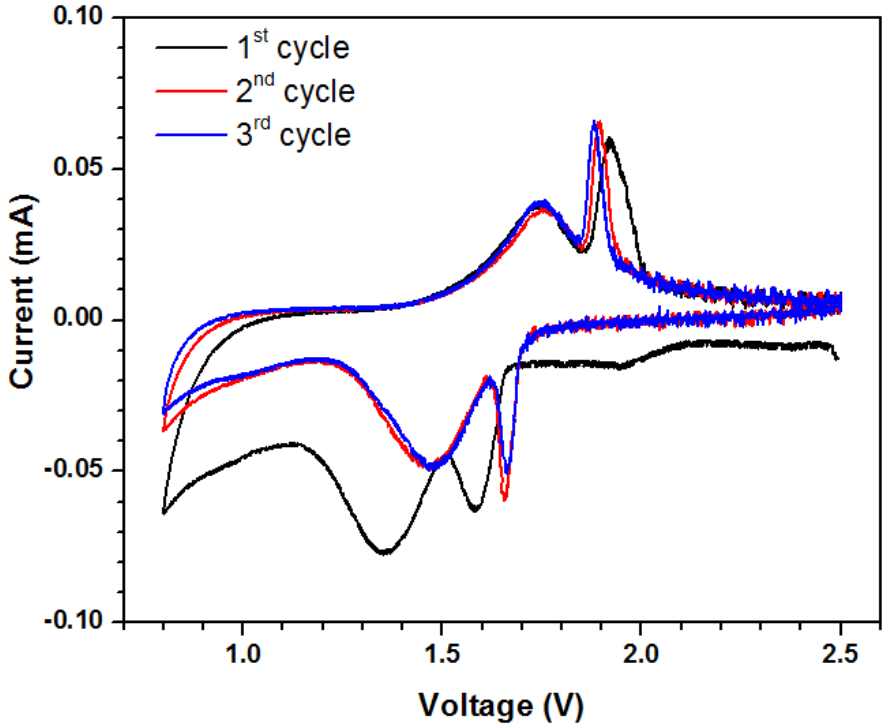


**Figure 2.9** Cyclic voltammtry of the Te/C composite electrode in the initial three cycles at a scan rate of 0.1 mV/s between 0.8 V and 2.5 V.

### 2.4.2 Cyclic voltammtry

Aside from charge/discharge profiles, cyclic voltammetry (CV) actually reveals more details about the electrochemical reaction during the lithiation/delithiation process. Figure 2.9 demonstrates the CV of the Te/C composite at a scan rate of 0.1 mV/s between 0.8 V and 2.5 V. Two redox couples are observed, with the reduction/oxidation peaks locating at 1.6/1.9 V, and 1.4/1.7 V separately, which is in good agreement with the double slope plateaus of charge/discharge curves in Figure 2.8b. The small reduction peak at 1.95 V, which disappears in the subsequent cycles, can be attributed to the formation of solid electrolyte interphase (SEI) film caused by the decomposition of electrolyte.

After first cycle, the two cathodic peaks shift to a higher voltage, while the anodic peaks shift slightly to lower voltage, reducing the potential hysteresis for lithiation and delithiation. The reduction of overpotential after first cycle has been observed in many high capacity electrodes, which is believed to be associated with the relaxation of stress/strain induced by volume expansion after first lithiation through deformation[32]. Moreover, the stable cathodic/anodic peaks after first cycle imply a high cycling stability.

### 2.4.3 Cycling stability

The cycling performance of Te/C composite is investigated by galvanostatic charge and discharge curves of the Te/C composite electrodes between 0.8 V and 2.5 V at a current density of 50 mA/g for 1000 cycles, as shown in Figure 2.9. The Te/C composite provides a volumetric capacity of 2022 mAh/cm$^3$, corresponding to a specific capacity of 324 mAh/g in the first delithiation process, which is close to the theoretical capacity of Te ($Li_2Te$: 419 mAh/g ). As the same group element with sulfur and selenium, although the specific capacity of tellurium/porous carbon composite is not as high as sulfur (($Li_2S$:1672 mAh/g)) and selenium ($Li_2Se$:675 mAh/g), the higher density provides tellurium a high volumetric capacity (2621 mAh/cm$^3$ based on density of 6.24 g/cm$^3$), which is comparable to that of selenium (3253 mAh/cm$^3$ based on density of 4.82 g/cm$^3$) and sulfur (3467 mAh/cm$^3$ based on density of 2.07 g/cm$^3$).

In addition, a reversible volumetric capacity of 1400 mAh/cm$^3$ (224 mAh/g) can be still retained even after 1000 cycles, with the Columbic efficiency always approaching up to 99% except for the first cycle, indicating an excellent cycling

stability The high irreversible capacity of the first cycle can be attributed to the electrolyte decomposition to form the solid electrolyte interphase (SEI) at the electrode surface and irreversible intercalation of lithium into the carbon matrix.

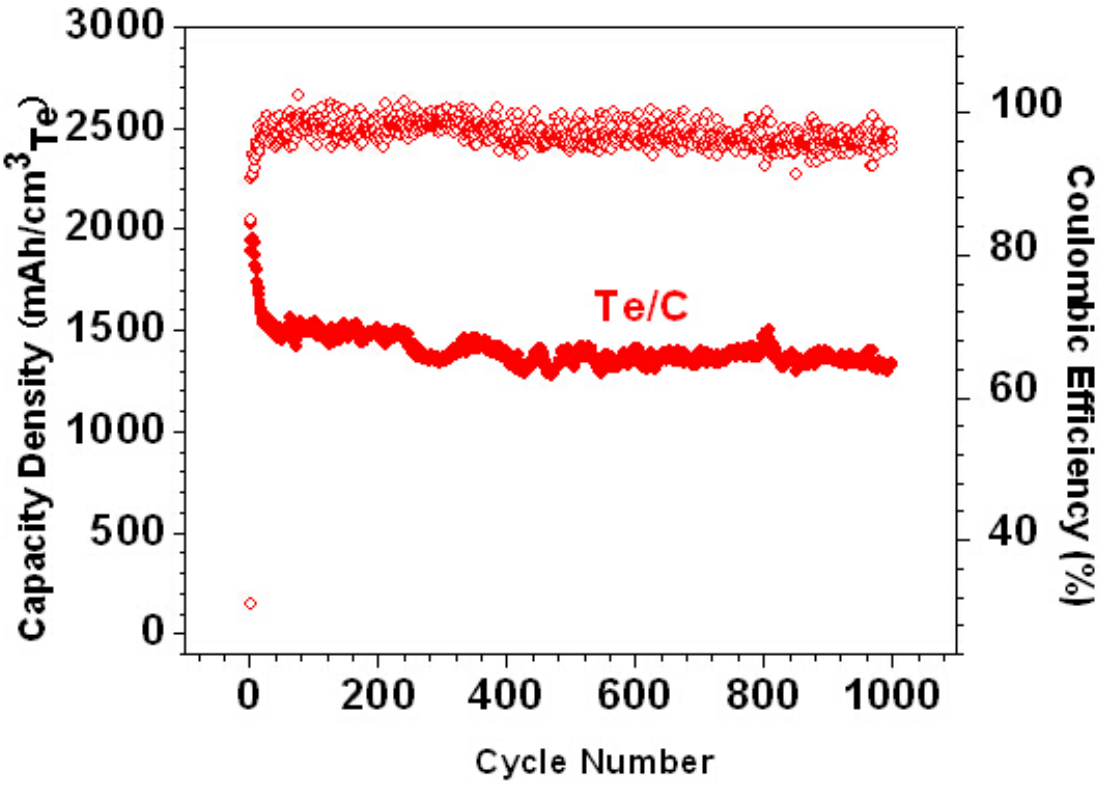


**Figure 2.10** Cycling performance and Coulombic efficiency of the Te/C composite electrode between 0.8 V and 2.5 V at a current density of 50 mA/g.

For comparison, the cycling stability of pristine Te electrode is also tested under the same electrochemical condition, which, however, suffered severely from rapid capacity fading。 The capacity retaining is only 7% of the initial capacity after merely 20 cycles. The poor cycling stability of pristine Te electrode indicates that pure tellurium suffers from capacity fading and may not be used in battery directly.

Therefore, after mechanical confinement and chemical stabilization of tellurium in the supporting carbon host, the Te/C composite possesses superior electrochemical performance with a high volumetric capacity and long cycle life.

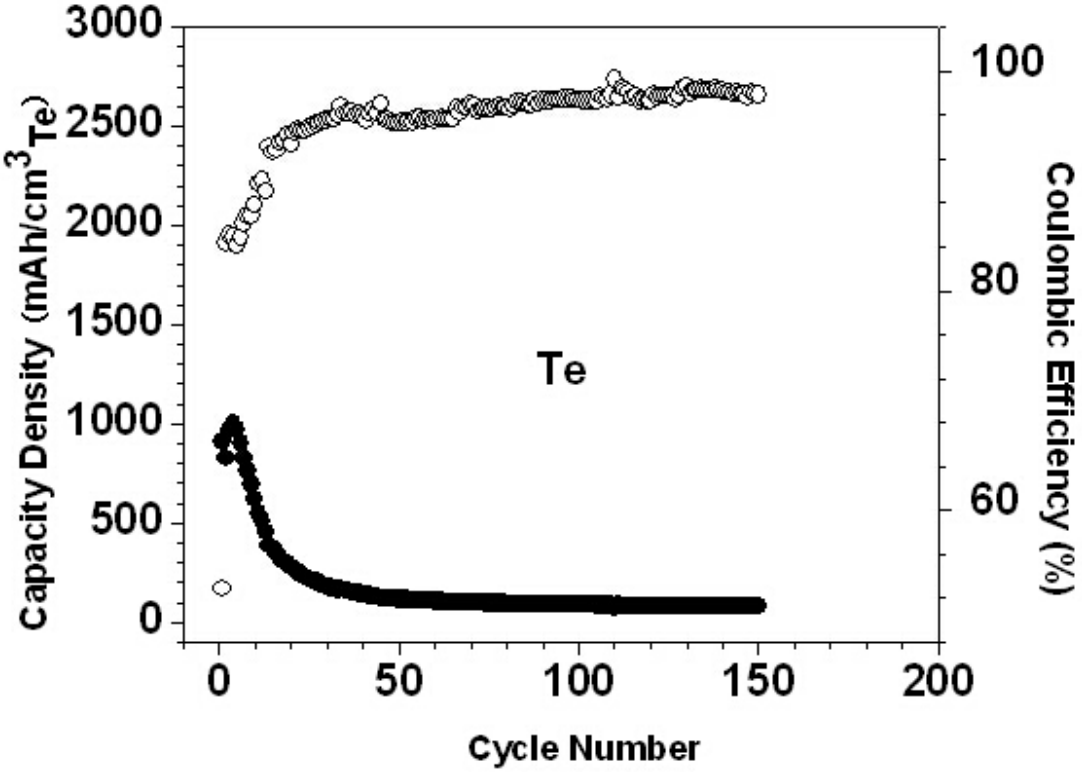


**Figure 2.11** Cycling performance and Coulombic efficiency of the pristine Te electrode between 0.8 V and 2.5 V at a current density of 50 mA/g.

2.4.4 Ratability

In addition to the good cycling stability, the Te/C electrode also displays a high rate capability. As shown in Figure 4c, when the current density increases from 50 to 1000 mA/g and 2000 mA/g, the volumetric capacity of the Te/C composite retains about 47% and 35% of capacity at 50 mA/g, respectively. Even when the Te/C composite is charged/discharged at 4000 mA/g, 17% capacity retention can still be

obtained. The superior volumetric capacity, high Columbic efficiency, long cycle life and good rate capability of Te/C composite demonstrates that tellurium is a promising electrode material candidate for Li-ion batteries, especially in large-scale energy storage applications.

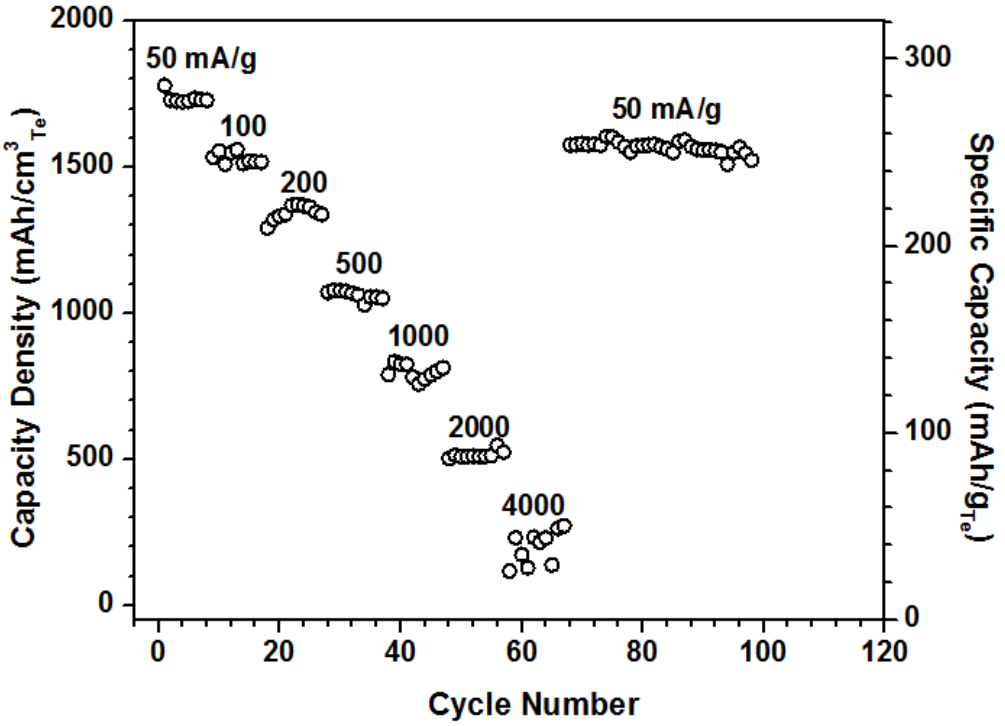


**Figure 2.12** Rate capability of the Te/C composite electrode in Li-Te batteries.

2.4.5 GITT

To investigate the reaction kinetics of Te/C composite at different lithiation/delithiation states, the over potential and reaction resistance of Te/C electrodes during charge/discharge were analyzed using the galvanostatic intermittent titration technique (GITT). During the GITT measurements, the Te/C electrodes were charged/discharged by a series of constant current pulse of 50 mA/g with equal duration period of 0.25 h. Following each pulse, the cells were left at open circuit

state for 6 h to reach the equilibrium potentials. Figure 2.13 demonstrates the potential response of Te/C electrode during GITT measurement in Li-ion batteries. The dotted-lines represent the equilibrium open circuit potentials (OCPs).

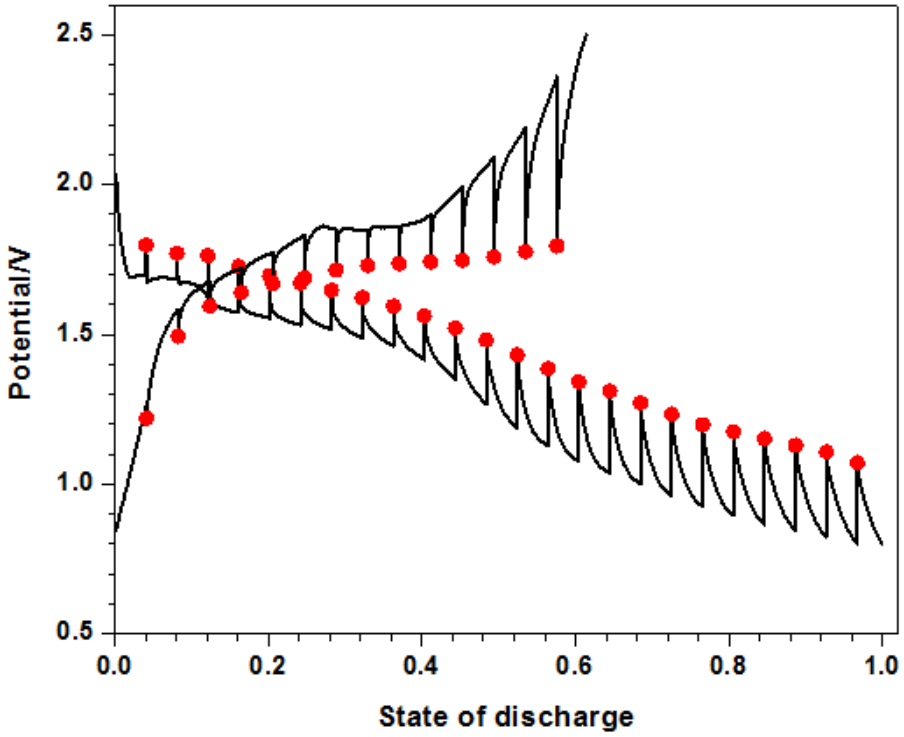


**Figure 2.13** Potential response of the Te/C composite electrode during GITT measurement.

The reaction resistance at different Li ion insertion and extraction levels is also calculated by dividing the over potential by the pulse current (Figure 2.14). The overpotential and reaction resistances of Te/C electrode shows two state increases with state of charge/discharge. For lithiation, the reaction resistance level-off after 50% of discharge, while the resistance rises expeditiously at the end of charge. The different behavior of reaction resistance between charge and discharge may be

attributed to the electronic contact resistance that decreases when volume expansion during lithiation and increases with volume contraction during delithiation.

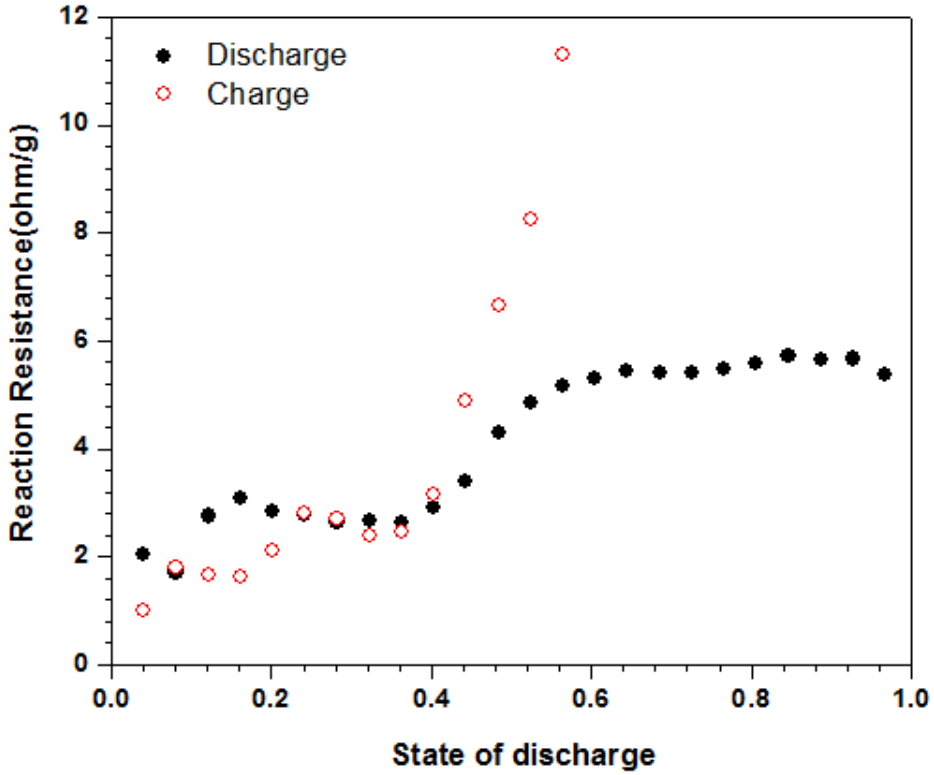


**Figure 2.14** Reaction resistance of the Te/C composite electrode during GITT measurement.

*2.5 Summary*

In summary, a novel tellurium/porous carbon (Te/C) composite is synthesized at a high temperature of 600 $^{o}$C under vacuum. The designed Te/C composite is employed, for the first time, as electrode material in lithium-ion batteries, which exhibits excellent electrochemical performance in commercialized carbonate-based electrolyte. Owing to the physical confinement and chemical stabilization of tellurium

in the supporting carbon matrix, the Te/C electrode can deliver a reversible volumetric capacity of 1400 mAh/cm$^3$ (224 mAh/g) and a high Coulombic efficiency near 99% over up to 1000 cycles without any further capacity decay. The high volumetric capacity, long cycle life, excellent Coulombic efficiency and good rate capability of Te/C composite demonstrates that Li-Te batteries are promising candidates for applications in large-scale and high-energy storage.

# Chapter 3: In situ TEM study of electrochemical sodiation and potassiation of carbon nanofibers

Ying Liu, Feifei Fan, Jiangwei Wang, Yang Liu, Hailong Chen, Katherine L. Jungjohann, Yunhua Xu, Yujie Zhu, David Bigio, Ting Zhu and Chunsheng Wang, *Nano Letter*, **2014**, 14, 3445

## *3.1 Introduction*

The large-scale storage of electrical energy for applications in electrical grids requires battery systems with high energy density and low cost. During the past decade, great effort has been devoted to Li-ion batteries (LIBs)[70,71]. However, the limited energy density and high cost still hinder the wide usage of LIBs to store large amounts of electrical energy from intermittent renewable sources such as solar and wind energy. Recently, batteries based on other alkali-metals, such as Na-ion batteries (NIBs) and K-ion batteries (KIBs)[10-12], have attracted great attention, owing to their comparatively high natural abundance and low cost[10,12-14]. Considering the similar chemical properties of Li, Na and K, the anode and cathode materials used in LIBs are being investigated for their applications in NIBs and KIBs in the past few years.

The potential anode materials for NIBs include carbonaceous materials, Sn, Sb, and metal oxides[10,13,14,34-38]. Among these candidates, carbonaceous materials[11,39-45] are most promising, given their successful applications in commercial LIBs and particularly low cost, natural abundance, small volumetric expansion during alloying with alkali-metals, in contrast to other anode materials such as Sn[36]. Graphite has been used as the anode of current commercial LIBs with a theoretical capacity of 372 mAh/g[46]. However, only a small amount of Na ions can be stored in the graphite anode of NIBs. Such a limitation has been often attributed to the higher intercalation

energy barrier of Na ions[10,11,47]. So far, the highest capacity for carbonaceous anodes reported in NIBs is about 300 mAh/g in hard carbon, whose usage is severely limited by its poor cyclability[45].

Recently, the disordered or amorphous carbon materials were found to exhibit much improved cyclability[11,41,48]. For example, the disordered hollow carbon nanowires showed a reversible capacity as high as 251 mAh/g with 82.2% capacity retention after almost 400 sodiation-desodiation cycles[41], which is much better than hard carbon[42,45]. Moreover, carbon is often used to enhance electron conduction in anodes or cathodes of LIBs and NIBs, as well as to support other active materials in high-capacity nanocomposite anodes for LIBs and NIBs[49-55].

Except research and progress in lithium-ion batteries and sodium-ion batteries, the designing of potassiation-ion batteries has attracted a lot of interest, due to the potential excellent insertion/extraction characteristics of potassiation ion into the active materials[72]. Moreover, the potential of potassium anode and lithium anode are close to each other, approximately the same with merely a 0.12 V difference, which is the closest one to that of lithium anode. Therefore, potassium ion batteries possess no disadvantages compared with its lithium ion batteries. However, there is much less attention paid to this type of rechargeable batteries. Recently, the Prussian blue electrode was reported to be used as cathode in potassium ion batteries, using nickel hexacyanoferrate nanoparticles electrode as cathode and aqueous solution as electrolyte[10-12]. This open framework structure guarantees the cathode with long cycle life, high power, and good energy efficiency. Whereas, so far, there are no published literatures can be found on the anode sides for the potassium ion batteries. And the

application of the carbon-based anodes in KIBs remains largely unexplored, compared with their LIB and NIB counterparts. Therefore, it is essential to understanding the electrochemical reactions and associated structure-property relationships of carbon-based anodes during sodiation and potassiation, thereby paving the way for future development of the novel carbon-based or carbon-supported nanocomposite anodes for NIBs and KIBs.

In this work, the electrochemical behavior and microstructure evolution of carbon nanofibers (CNFs) during Na and K insertions are studied in real time by using a nanoscale battery setup inside a transmission electron microscope (TEM) and electrochemical tests. The CNFs are hollow and consist of a bilayer wall with an outer layer of disordered-carbon (*d*-C) enclosing an inner layer of crystalline-carbon (*c*-C). With such bilayer CNFs, the sodiation and potassiation responses of *c*-C and *d*-C are directly compared at the same time. Longitudinal cracks are frequently observed near the *c*-C/*d*-C interface during sodiation and potassiation. Their chemo-mechanical origin is revealed by a computational modeling study using Finite element simulations. In addition, an in situ TEM study of amorphous Si (*a*-Si) coated CNFs is also conducted to further evaluate the mechanical confinement effect on sodiation and potassiation.

### *3.2 In situ TEM setup*

Figure 3.1 presents a schematic illustration of the solid cell that enables the electrochemical experiments of individual carbon Nanofibers in Na-ion batteries and K-ion batteries. The carbon nanofibers (CNFs) is a commercial product (PR-19) ordered from the Pyrograf Products, Inc. The nano-sized electrochemical cell in side

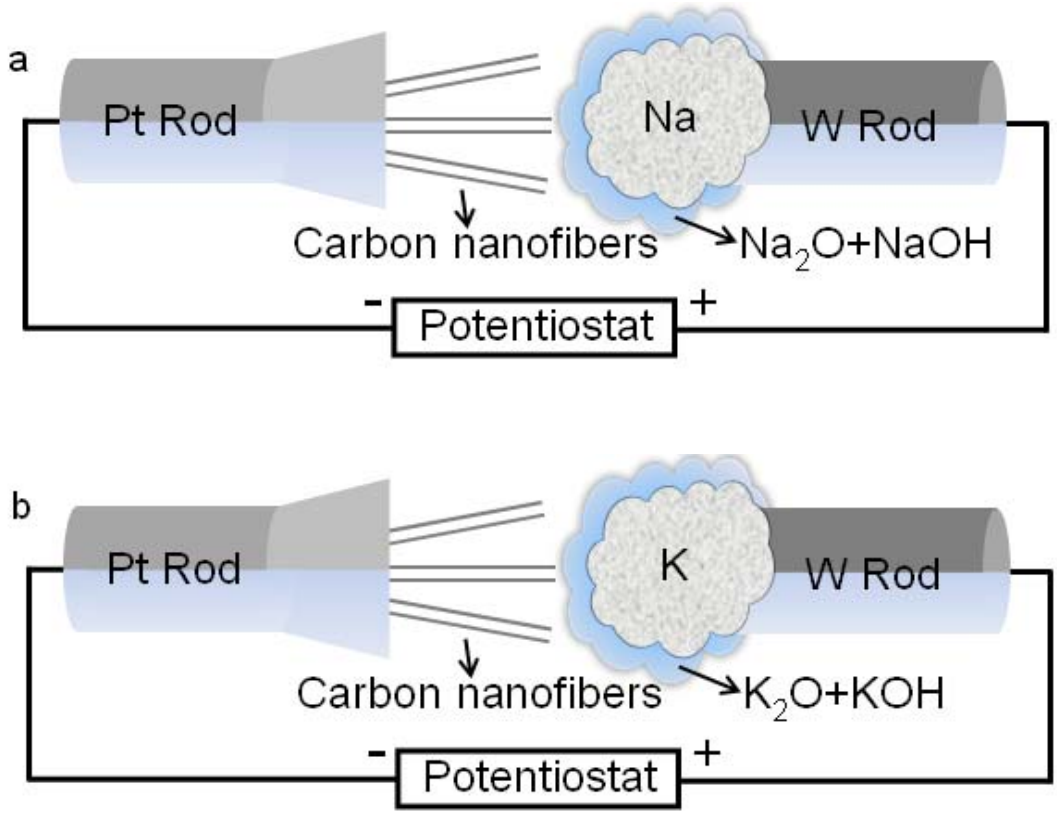


**Figure 3.1** Schematic illustration of the solid cell that enables the electrochemical experiments of individual carbon Nanofibers. (a) Na-ion batteries. The working electrode is carbon nanofibers dispersed on a platinum (Pt) rod, and the counter electrode is bulk Na metal on a tungsten (W) rod. The solid electrolyte is naturally grown sodium oxide and hydroxide ($Na_2O$ and NaOH) on the sodium metal. (b) K-ion batteries. The working electrode is carbon nanofibers dispersed on a platinum (Pt) rod, and the counter electrode is bulk K metal on a tungsten (W) rod. The solid electrolyte is naturally grown potassium oxide and hydroxide ($K_2O$ and KOH) on the potassium metal.

of TEM consisted of a working electrode of CNFs dispersed on a platinum (Pt) rod, a counter electrode of bulk Na metal on a tungsten (W) rod for Na-ion batteries and bulk K metal on a tungsten (W) rod for K-ion batteries, and a solid electrolyte of naturally grown sodium oxide and hydroxide ($Na_2O$ and NaOH) on the sodium metal for Na-ion batteries and naturally grown potassium oxide and hydroxide ($K_2O$ and KOH) on the sodium metal for K-ion batteries. In a typical experiment, fresh sodium or potassium metal was scratched off from a freshly cut surface of sodium or potassium bulk with the W rod inside the glove box filled with helium.

The working electrode and counter electrode were mounted onto the Nanofactory TEM-scanning tunneling microscopy (STM) holder in the glove box, which was then transferred in a homemade sealed plastic bag filled with dry helium and loaded into the TEM column. The sodium metal or potassium metal were exposed to the air for about 2 s during the holder loading process, and as a result, a layer of sodium oxide and sodium hydroxide mixture or potassium oxide and potassium hydroxide mixture were grown on the sodium or potassium surface, which was served as the solid electrolyte for sodium ions transport and potassium ions transport. During the in situ TEM experiments, potentials of -0.5 to -2 V were applied to the CNFs with respect to Na/K metal to drive sodiation/potassiation (Na/K insertion) and +2 to +4 V for desodiation/depotassiation (Na/K extraction).

### *3.3 Characterization of carbon Nanofibers*

Figure 3.2 shows the typical morphology of a pristine hollow CNF, which involves a bilayer structure, i.e., a *d*-C outer layer enclosing a *c*-C inner layer. The

bilayer CNF is a commercial product (PR-19) ordered from the Pyrograf Products, Inc. The diameter of CNFs is typically in the range of 120 - 300 nm and the length is about tens of micrometers. The bilayer structure is clearly seen from a zoom-in image in Figure 3.2b, *i.e.*, the *c*-C inner layer with a dark contrast and the *d*-C outer layer with a light contrast.

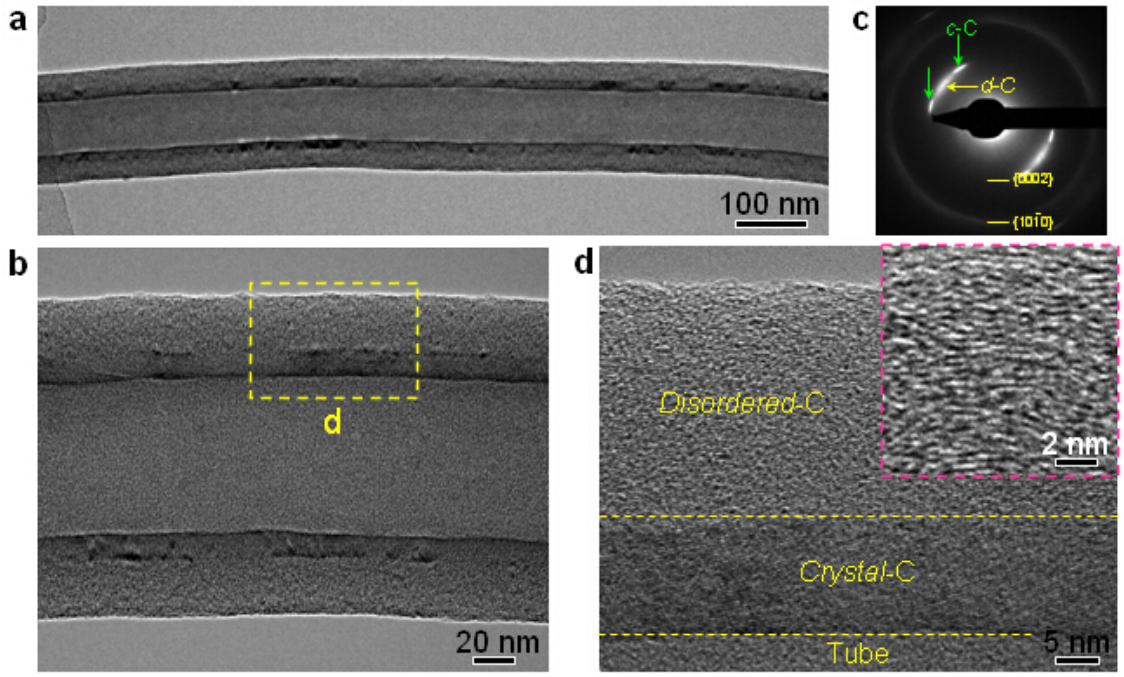


**Figure 3.2** Typical morphology and structure of a pristine hollow carbon nanofiber (CNF) with a bilayer wall. (a-b) The wall of CNF consists of a *d*-C/*c*-C bilayer. (c) Electron diffraction pattern (EDP) of the bilayer CNF. Two different kinds of spots are shown in the EDP for the {0002} plane of CNF. The two sets of sharp spots (indicated by green arrows) correspond to the diffraction of *c*-C, while the diffuse spots (indicated by yellow arrows) the diffraction of *d*-C. (d) High resolution TEM (HRTEM) image of the CNF, with the inset showing the local graphite lattice fringes in the *d*-C layer.

Figure 3.2d shows a high resolution TEM (HRTEM) image of the bilayer structure. In the *d*-C layer, the local domains of graphitic lattice fringes (inset in Figure 3.2d) are clearly visible, implying *d*-C is not completely disordered. Namely, *d*-C consists of an assembly of many few-layered graphene patches that are not perfectly aligned in the same orientation. Such a locally ordered structure in *d*-C is similar to that in hard carbon consisting of stacked graphite layers (termed as graphite nanocrystallites) with micro-voids in between[45,47].

The local crystalline order in *d*-C is also reflected in the electron diffraction pattern (EDP), as shown in Figure 3.2c. It is interesting to note that two different kinds of spots are shown in the EDP for {0002} planes. The two sets of sharp spots (indicated by green arrows in Figure 1c) arise from the diffraction of *c*-C, while the diffuse spots from *d*-C (indicated by the yellow arrow in Figure 3.2c). Note that the diffuse diffraction spots of *d*-C are different from the diffraction halo of the pure amorphous phase, which further confirms that the *d*-C layer is not fully disordered. The unique bilayer structure in CNFs allows us to directly compare the behaviors of *c*-C and *d*-C during Na or K insertion.

### *3.4 Electrochemical tests result and discussion*

The CNF anode was prepared by mixing 85 wt% CNFs powder, 15 wt% polyvinylidene difluoride (PVDF) dissolved in N-methyl-2-pyrrolidone (NMP) to form slurry. Then, the electrode was made by spreading slurry onto a copper current collector and dried at room temperature overnight followed by heating at 100 $^{o}$C in a vacuum oven overnight. The cells were assembled in an argon-filled glove box, with

CNFs as the working electrode, sodium metal or potassium metal as the counter/reference electrode, 1 M $NaPF_6$ or 1 M $KPF_6$ dissolved in a mixture of ethylene carbonate and dimethyl carbonate (EC/DMC, 1:1 by volume) as the electrolyte for Na-ion battery and K-ion battery, correspondingly, and Celgard®3501 (Celgard, LLC Corp., USA) as the separator. The galvanostatic charge/discharge curve was tested at a voltage range of 0-1.2 V (vs $Na^+$/Na or $K^+$/K) at a constant current rate of 50 mA/g, using an Arbin battery test station (BT2000, Arbin Instruments, USA) under ambient temperature.

### 3.4.1 Charge/discharge curve

Galvanostatic discharge-charge cycling is performed to directly measure the capacity of the bilayer CNF electrode during sodiation and desodiation at a constant current rate of 50 mA/g in a coin cell (Figure 3.3).

Since the capacity of *c*-C during Na insertion/extraction is extremely small[47], and Na ions are mainly stored in *d*-C rather than *c*-C, as suggested by the *in situ* TEM electrochemical studies in the following parts, the specific capacity of CNFs anode is calculated based on the weight of *d*-C only. To estimate the weight ratio of *d-C* and *c-C* accurately, we notice that the structure of bilayer CNFs are uniform along the axial direction. We have measured the diameters of inner tube, bilayer interface and outer surface in more than 30 bilayer CNFs and calculated the weight ratio of *d-C*:*c-C* by:

$$Weightratio = \frac{r_{outer}^2 - r_{interface}^2}{r_{interface}^2 - r_{inner}^2}$$

where, $r_{inner}$, $r_{interface}$ and $r_{outer}$ are the diameters of inner tube, bilayer interface and outer surface, respectively. The measured weight ratio of *d-C*:*c-C* are ranging in 2.87-

3.21 with the average value of 3.02, which is about ~75% of the total mass of CNFs.

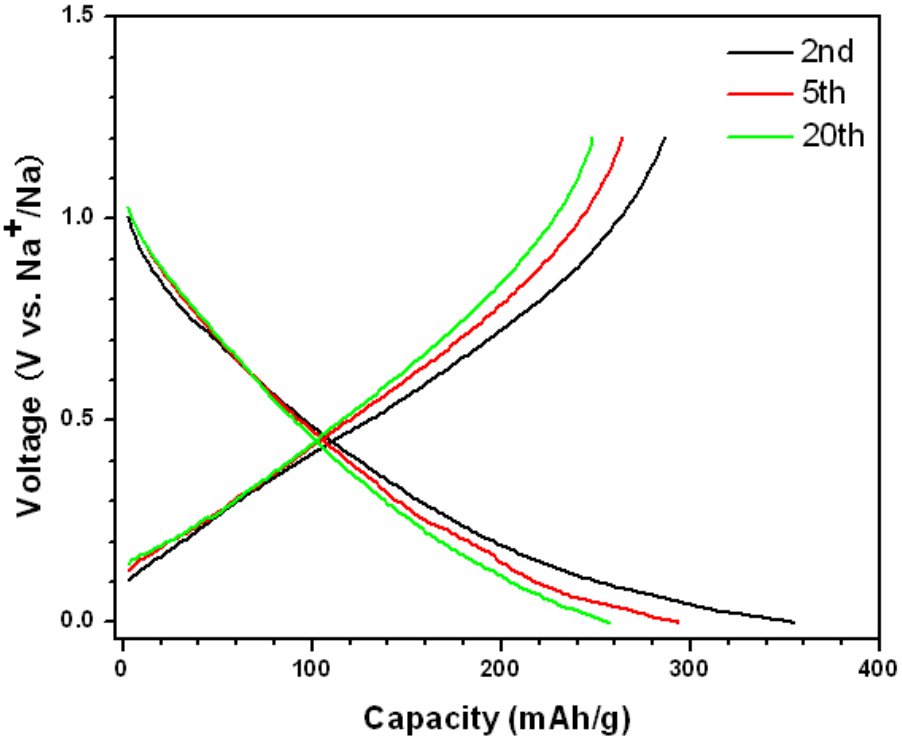


**Figure 3.3** Charge-discharge curves measured for bilayer CNF electrodes in the second, fifth and twentieth cycle in a coin cell for Na-ion battery. The electrodes are tested in the voltage range of 0-1.2 V (vs $Na^+/Na$) at a current density of 50 mA/g, with the electrolyte of 1 M $NaPF_6$ dissolved in the mixture of EC+DMC (1:1 by volume). The specific capacity is calculated based on the mass of *d*-C, which is about 75% of the total mass of CNFs.

For Na insertion into the carbon based anodes, there are mainly two insertion mechanisms involved: 1) Insertion of Na between the graphene layers corresponding to the slope-shaped voltage profile; 2) Insertion of Na into the micropores of carbon corresponds to a plateau at the lowest potentials[11]. Since the micropores in the bilayer CNFs is limited, thus the discharge-charge profile in Figure 3.3 exhibits only a

monotonous slope in the voltage range of 0 - 1.2 V, which likely corresponds to the insertion of Na ions between the graphene layers in *d*-C[11]. This consists with our TEM results as follows, where Na ions insert in between the graphene layers of stacked graphite patches in *d*-C[41].

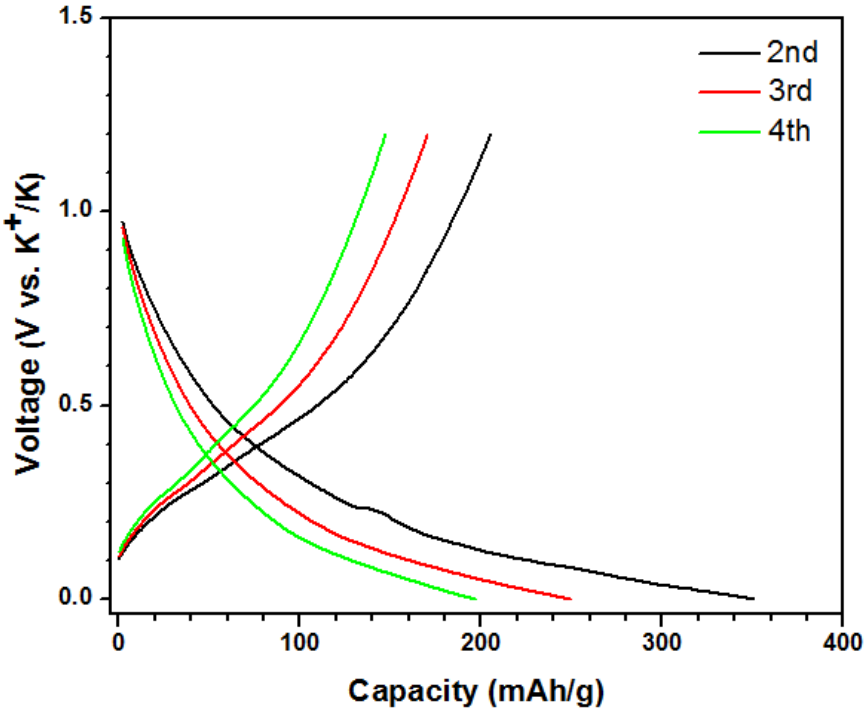


**Figure 3.4** Charge-discharge curves for bilayer CNF electrodes in the second, third and fifth cycle in a coin cell for K-ion battery. The electrodes are tested in the voltage range of 0-1.2 V (vs $K^+/K$) at a current density of 50 mA/g, with the electrolyte of 1 M $KPF_6$ dissolved in the mixture of EC+DMC (1:1 by volume). The specific capacity is calculated based on the mass of *d*-C, which is about 75% of the total mass of CNFs.

The bilayer CNF electrode exhibits similar monotonous slope-shaped discharge/charge curve in K-ion batteries in the voltage range of 0 - 1.2 V (vs $K^+/K$), as shown in Figure 3.4. It has been well accepted that there are mainly two insertion mechanisms involved for Na insertion into the carbon based anodes: 1) Insertion of

Na between the graphene layers corresponding to the slope-shaped voltage profile; 2) Insertion of Na into the micropores of carbon corresponding to a plateau at the lowest potentials[11]. Thus, similar to NIBs, this monotonous slope is likely corresponding to the insertion of potassium ions between the graphene layers in *d*-C. This consists with our TEM results as follows, where K ions insert in between the graphene layers of stacked graphite patches in *d*-C.

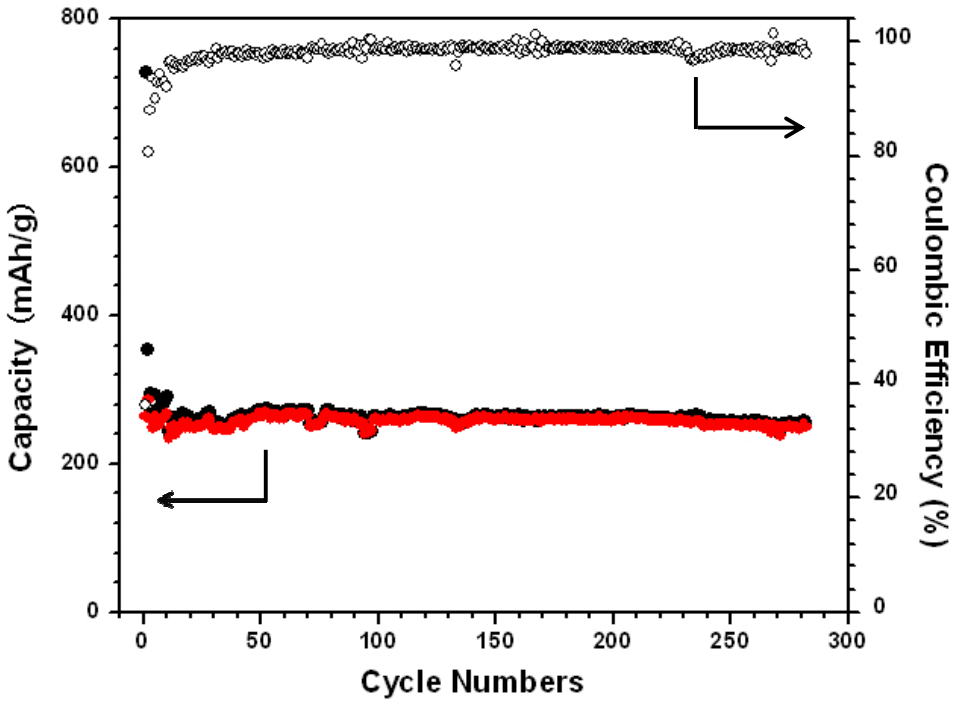


**Figure 3.5** Cycling stability and Coulombic efficiency measured for bilayer CNF electrodes in a coin cell for Na-ion battery.

### 3.4.2 Cycling stability

Figure 3.5 shows the capacity stability and Coulombic efficiency of CNFs anode during Na insertion and extraction. The initial discharge and charge capacities are 728 and 263 mAh/g, respectively, giving a Coulombic efficiency of 36%. The large irreversible capacity in the first cycle is likely due to the electrolyte

decomposition to form the solid electrolyte interphase (SEI) at the electrode surface, as well as irreversible insertion of Na into graphitic layers. The capacity decay occurs primarily in the first few cycles, which is possibly attributed to the SEI stabilization, volume adjustment during Na ions insertion/extraction and partially irreversible Na ions insertion[11,41]. After initial adjustment cycles, a reversible capacity of 245 mAh/g is stably maintained with a Coulombic efficiency approaching 98%, which is in good agreement with other reported results on sodiated disordered carbon[41,73]. Since the inactive *c-C* can function as a build-in current collector, this bilayer CNFs shows excellent cycling stability, with 99% capacity retention after 280 cycles, indicating great potential of *d-C* in the application for NIBs.

Figure 3.6 shows the capacity stability and Coulombic efficiency of CNFs anode during K insertion and extraction. The initial discharge and charge capacities are 705 and 300 mAh/g, respectively, giving a Coulombic efficiency of 43%. The large irreversible capacity in the first cycle is due to SEI formation, as well as irreversible insertion of K into graphitic layers. The capacity decays very fast in the first few cycles, which is possibly attributed to the large K ions, SEI stabilization, volume adjustment during K ions insertion/extraction and partially irreversible K ions insertion[11,41]. Although the cycling stability of CNFs electrode for K-ion battery at the same current rate is not as good as Na-ion battery, due to the kinetics problems of larger K ions, the electrochemical test suggest that *d-C* is capable to storage more K-ions, as confirmed by the following TEM results. And highly-disordered carbon might be a way for a better cycling stability for KIBs, since highly-disordered carbon possesses more defects than lower-disordered carbon, which can provide more sites

for potassium insertion. The potassiation of the bilayer CNFs indicates that *d*-C is a promising anode candidate for KIBs.

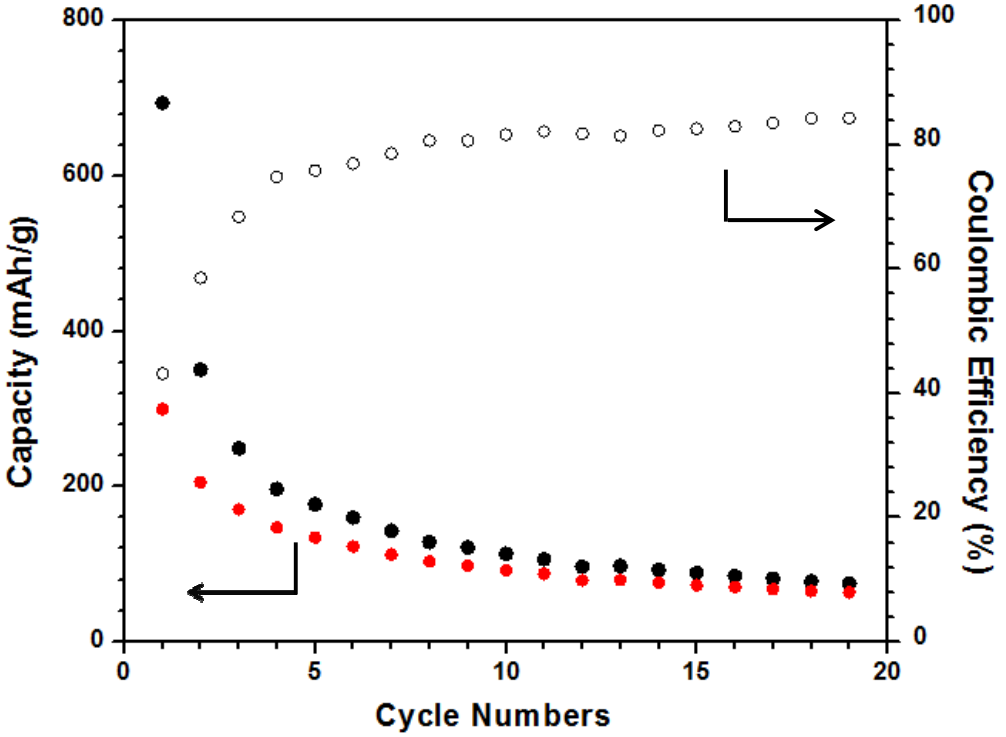


**Figure 3.6** Cycling stability and Coulombic efficiency measured for bilayer CNF electrodes in a coin cell for K-ion battery.

*3.5 In situ TEM tests result and discussion*

The in situ experiments of electrochemically-driven sodiation and potassiation of CNFs are conducted by using an all-solid nanobattery setup inside a TEM. The working electrode is carbon nanofibers dispersed on a platinum (Pt) rod, the counter electrode is bulk Na metal on a tungsten (W) rod for Na-ion batteries and bulk K metal on a tungsten (W) rod for K-ion batteries, the solid electrolyte is naturally grown sodium oxide and hydroxide ($Na_2O$ and NaOH) on the sodium metal for Na-

ion batteries and naturally grown potassium oxide and hydroxide ($K_2O$ and KOH) on the sodium metal for K-ion batteries. The details of the nanobattery setup and operation can be found in Figure 3.1.

To confirm the negligible effects of electron beam on electrochemical reactions, both beam-on and beam-blank experiments (as indicated in figure captions) are performed, showing qualitatively similar behaviors.

### 3.5.1 Geometry and structure change during sodiation

Figure 3.7 presents the microstructures of a hollow bilayer CNF before and after the beam-blank sodiation. For the pristine hollow CNF, its inner diameter is about 130 nm and wall thickness is about 63 nm (Figure 3.7c). After full sodiation, the inner diameter decreases to 116 nm and the outer diameter increases to 263 nm. As a result, the total wall thickness increases to 73.5 nm, owing to sodiation-induced volume expansion. In addition, sodiation causes an increase of the thickness of the *c*-C layer from 25.5 nm to 29 nm, which corresponds to an average radial and volume strain of 13.7% and 6%, respectively. Similarly, the thickness of the *d*-C layer increases from 37.5 nm to 44.5 nm, which corresponds to an average radial and volume strain of 18.7% and 18.7%, respectively.

Hence, the sodiated *d*-C exhibits about three times volume expansion of *c*-C, thus suggesting a much higher storage capacity of Na ions in *d*-C than *c*-C. Incidentally, a thin layer of $Na_2O$ (about 2~3 nm thick) is observed to quickly form on the CNF surface (Figure 3.7d) while the bulk sodiation is still ongoing, thus suggesting fast surface diffusion of Na on CNFs [74,75].

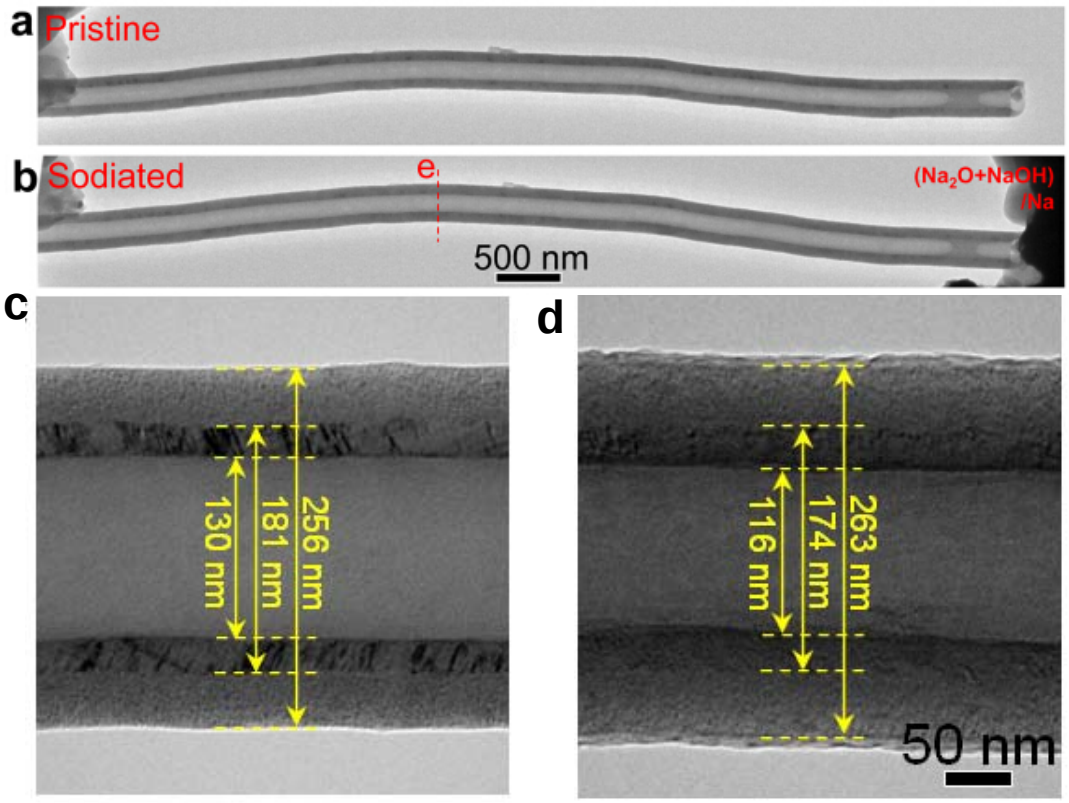


**Figure 3.7** Geometry and structure changes of a bilayer CNF during sodiation under a beam-blank condition. (a, c) Pristine CNF. (b, d) Sodiated CNF.

Figure 3.8 presents the line scan profiles across the CNF after sodiation, and the green arrows indicate the peak positions of Na and C intensity profiles. Na and C exhibit different spatial distributions, i.e., the Na intensity reaches a peak in the middle of the CNF wall and decreases gradually away from the peak, while the C intensity continually increases from the outer to the inner tube wall. Such difference indicates that the *c*-C and *d*-C have different capacities of storing Na ions, as further confirmed by EDPs (Figure 3.9).

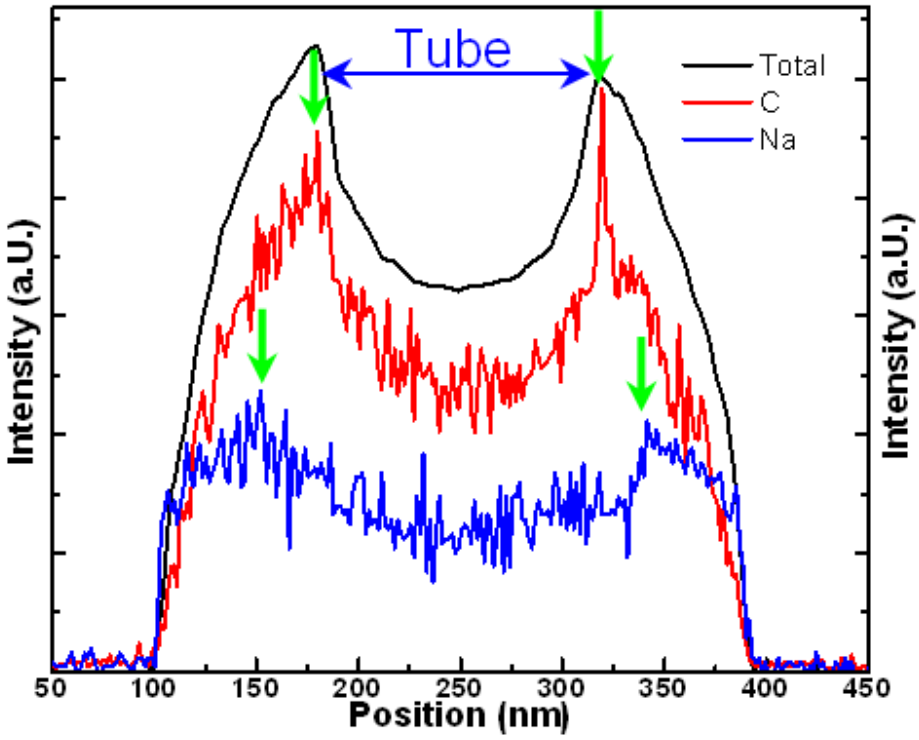


**Figure 3.8** The line scan profiles of C and Na across the CNF after sodiation. The green arrows point to the peak positions of Na and C intensity profiles.

The EDP of the pristine CNF shows a typical diffraction pattern of the bilayer CNF with an average {0002} plane spacing of 3.38 Å (Figure 3.9a), which is slightly larger than the theoretical spacing of {0002} plane of 3.35 Å. Such a difference is presumably induced by the partially disordered structure of *d*-C. After full sodiation, the diffraction pattern of {0002} planes splits into two sets with different lattice spacings (Figure 3.9b). For *c*-C, the average spacing of {0002} planes increases to 3.67 Å. This corresponds to an expansion of 8.6% between neighboring graphitic layers, which is slightly larger than that of lithiation (~ 7%)[75] and can be correlated to the larger size of Na ions[10]. In contrast, the average spacing of {0002} planes of *d*-C increases up to about 4.16 Å. This corresponds to an expansion of ~ 23% along [0002]

(i.e. *c* axis) direction, which is about three times that in the sodiated *c*-C.

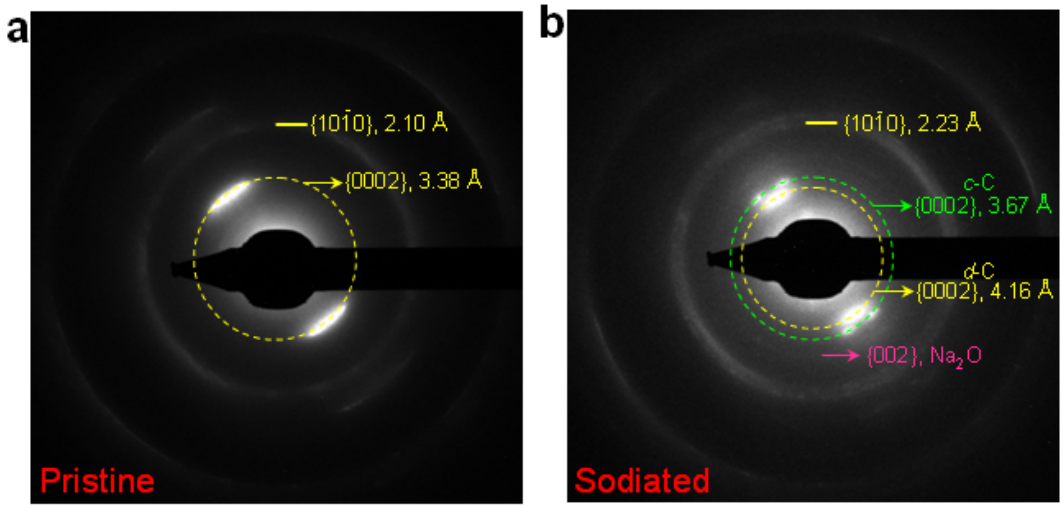


**Figure 3.9** Electron diffraction patterns (EDPs) of the CNF (a) before and (b) after sodiation. The average spacing of {0002} planes is about 3.38 Å in the pristine CNF. Two sets of patterns form after sodiation; the average spacing of {0002} planes in *c*-C and *d*-C increases to 3.67 Å and 4.16 Å, respectively.

The larger the increase of the *d*-spacing along *c* axis, the more Na ions the carbon system likely stored. However, the quantitative capacity of sodiation in *d*-C cannot be determined directly by our in situ TEM experiment, due to the difficulty of measuring the extremely small electric current. In addition, much less changes are observed in the lattice spacing of $\{10\bar{1}0\}$ planes (Figure 3.9), which indicates that Na ions are most likely inserted in between rather than within the graphitic layers. The EDP after sodiation is consistent with the line scan profiles in Figure 3.8, suggesting that more Na ions can be stored in *d*-C. Compared to *c*-C, the larger capacity of Na ions storage in *d*-C might originate from more defects existing in *d*-C, while the atomic-scale mechanism of Na ion accommodation warrants further study in future.

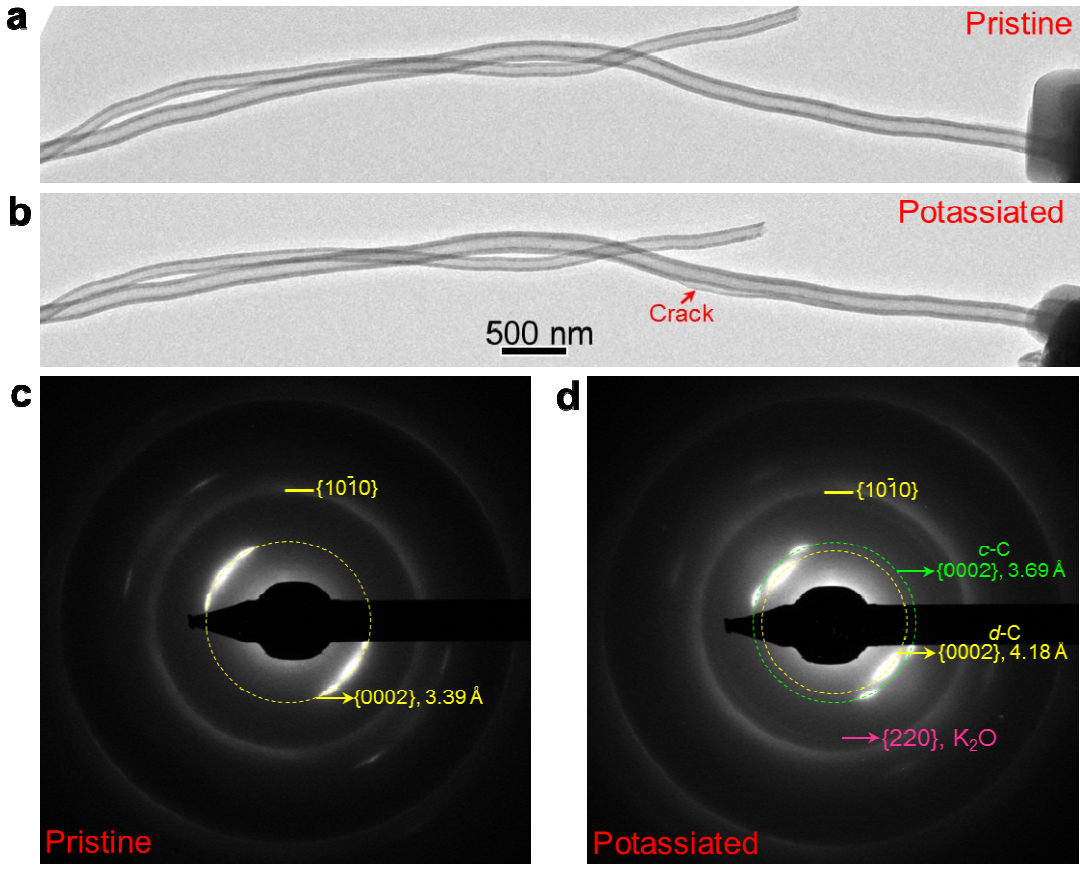


**Figure 3.10** Microstructure evolution of a bilayer CNF during potassiation. The experiment was conducted under beam-blank. (a-b) Morphologies of pristine and potassiated CNFs. A crack forms after full potassiation, as indicated by the red arrow in (b). (c-d) EDPs of the CNF before and after potassiation. For the pristine CNF, the average spacing of {0002} planes is about 3.39 Å. The EDP splits into two sets of patterns with different lattice spacings after potassiation. The average spacing of {0002} planes for *c*-C increases to 3.69 Å after full potassiation, while the one for *d*-C increases to ~ 4.18 Å.

Figure 3.10 presents the microstructure change of a hollow bilayer CNF before and after the beam-blank potassiation, which shows similar responses as CNF in sodiation. The average spacing of {0002} planes of *c*-C increases from 3.39 Å to ~

3.69 Å after potassiation, corresponding to an expansion of ~ 8.8% along *c* axis. While the average spacing of {0002} planes of *d*-C increases to ~ 4.18 Å after potassiation, corresponding to an expansion of ~ 24% along *c* axis, implying almost three times volume expansion of *d*-C than *c*-C after potassiation. Moreover, much less changes are observed in the lattice spacing of $\{10\bar{1}0\}$ planes (Figure 3.10), indicating that K ions are most likely inserted in between rather than within the graphitic layers.

Therefore, both sodiation and potassiation of the bilayer CNF indicate that *d*-C has a better capability of storing Na or K ions than *c*-C, which is desired for the anode of NIBs and KIBs.

### 3.5.2 Sodiation/potassiation induced cracks

Mechanical degradation in electrodes is usually an important cause of the irreversible capacity loss in rechargeable batteries[76]. Our in situ TEM study reveals the mechanical degradation through formation of interface cracks in bilayer CNFs during sodiation and potassiation.

Figure 3.11 shows an in situ TEM result of the sodiation-induced cracks in a bilayer CNF. The sample is tested under beam-on with a very weak electron beam. Upon sodiation, a crack nucleates from the contact point between the CNF and $Na_2O$/Na electrolyte, as indicated by red arrows in Figure 3.11b. As sodiation proceeds, the crack propagates from one end to the other end of the CNF along its axial direction (Figure 3.11c-d). Interestingly, crack initially nucleates on the upper wall of the CNF and then extends to its lower wall, which is likely caused by screw rotation of moving crack front around the axial direction, as shown in Figure 3.11e-g.

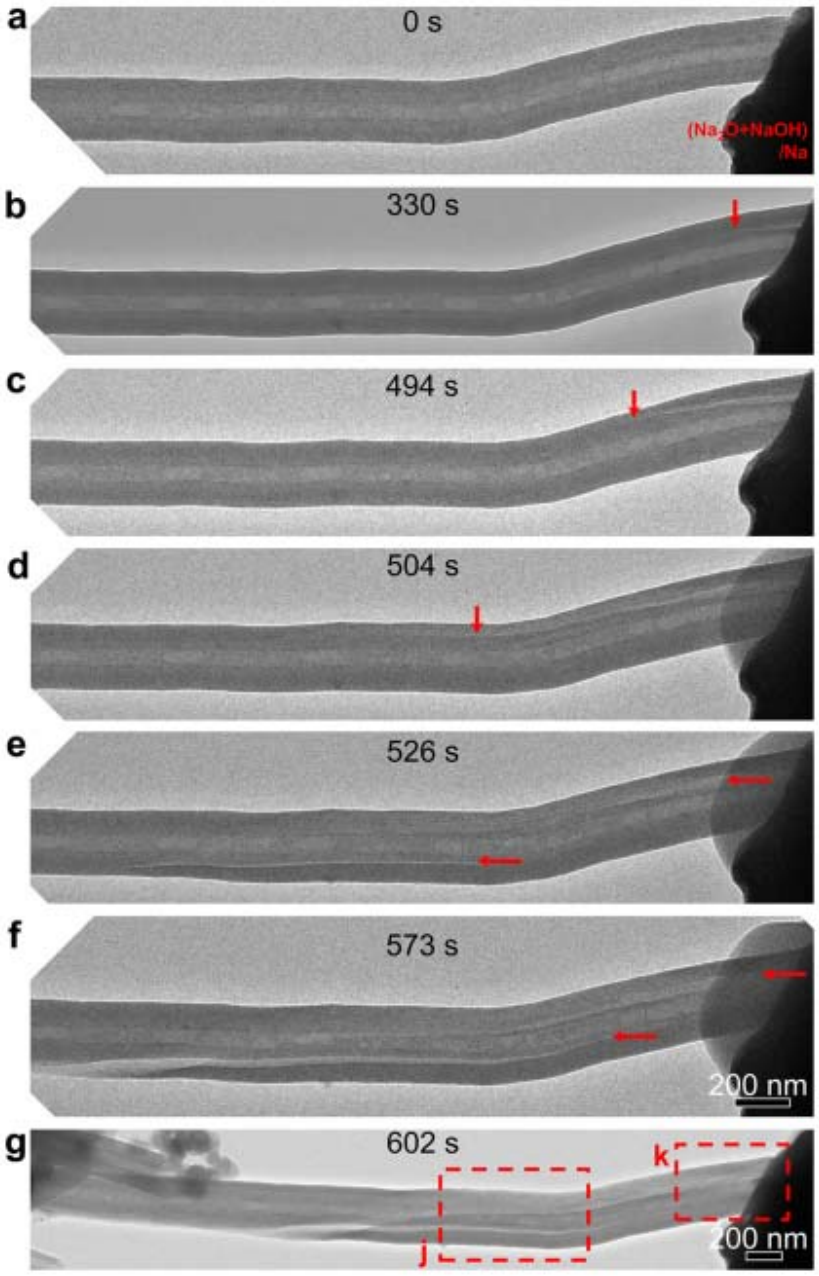


**Figure 3.11** Sodiation-induced crack nucleation and propagation in a hollow bilayer CNF under a beam-on condition with very weak electron-beam exposure. (a) Pristine CNF. (b-g) The dynamic process of the sodiation-induced crack nucleation and propagation. The red arrows indicate the crack and its propagation front.

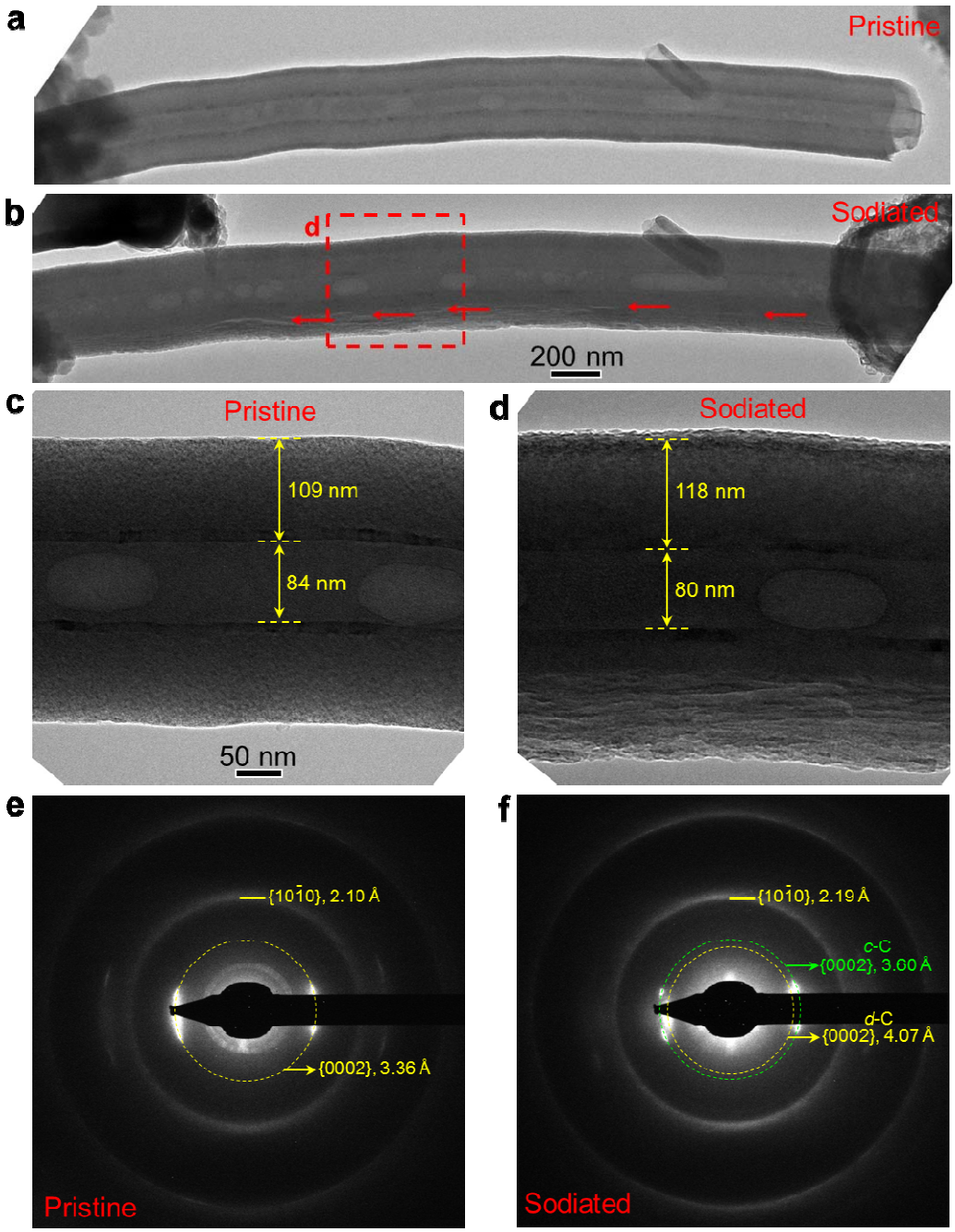


**Figure 3.12** Sodiation-induced cracks in a bilayer CNF under beam-on with very weak electron-beam exposure. (a) Pristine CNF. (b) Sodiated CNF with cracks formed. (c-d) Zoom-in images showing the cracks. (e-f) EDPs of the CNF before and after sodiation.

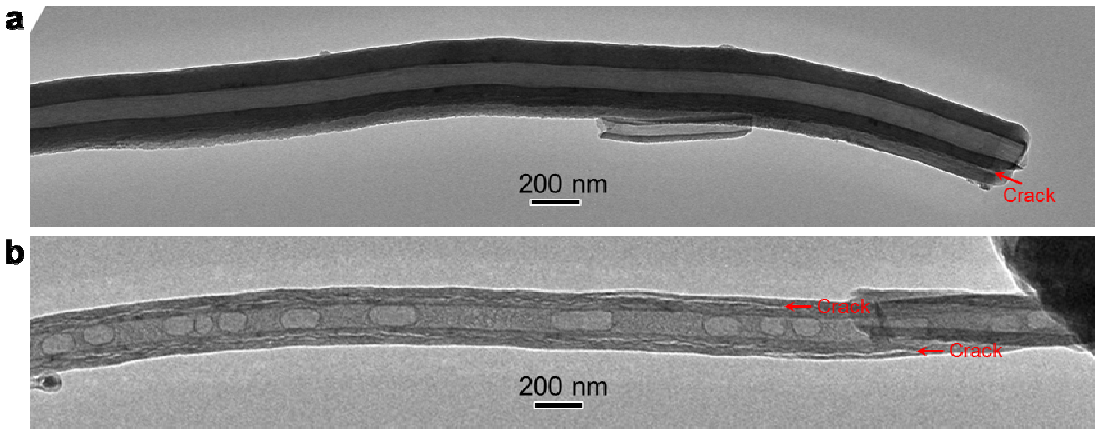


**Figure 3.13** Additional examples of crack formation in bilayer CNFs after sodiation. The experiments were conducted under beam-blank. The red arrows point to the cracks.

Such kind of sodiation-induced cracking is frequently observed (5 out of 6 samples) with either beam-on with very weak electron-beam exposure (Figure 3.11 and 3.12) or beam-blank (Figure 3.13) condition, thus suggesting the insensitivity of cracking to electron beam.

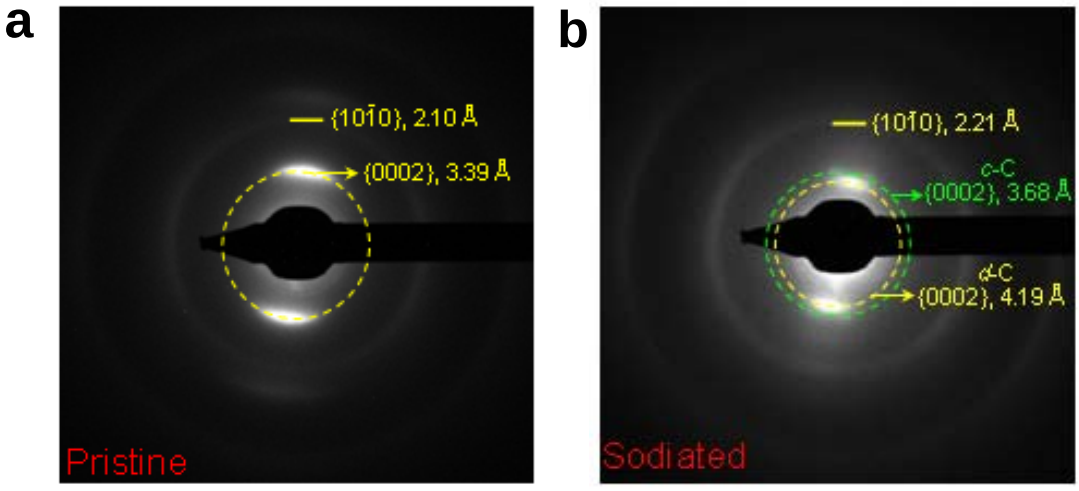


**Figure 3.14** EDPs of the CNF before and after the sodiation under beam on condition.

Similar to Figure 3.11f-g, a large increase in the spacing of {0002} planes is observed after sodiation (Figure 3.14a-b), from 3.39 Å to 4.19 Å from *d*-C and 3.68 Å for *c*-C. Figures 3.15a-b show the zoom-in images of longitudinal cracks, which are located at different places, but all close to the interface between the *c*-C and *d*-C layers. Figure 3.10 shows an in situ TEM result of potassiation of a bilayer CNF, where cracks near the interface are also observed.

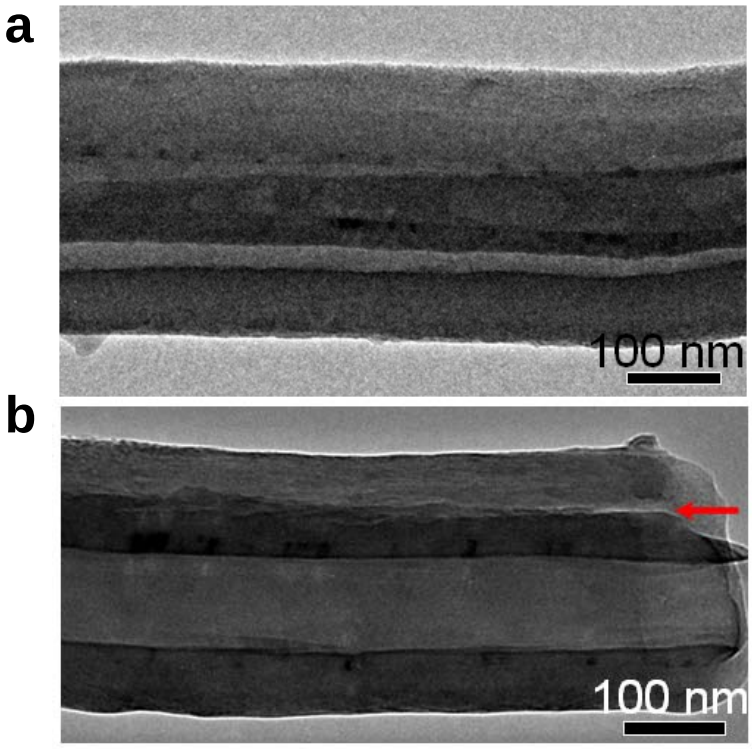


**Figure 3.15** Zoom-in images showing the cracks close to the *c*-C/*d*-C interface of CNF after sodiation under beam on condition.

In contrast, no cracking is observed during the sodiation of monolithic *d*-C CNFs, being either solid or hollow, as shown in Figure 3.16. Such different cracking behavior suggest that the unique bilayer structure, along with the hollow geometry, plays an important role in crack formation during sodiation and potassiation of CNFs.

Such interface cracking might be responsible for capacity fading in the initial charge/discharge cycles in Figure 3.5 and 3.6[74].

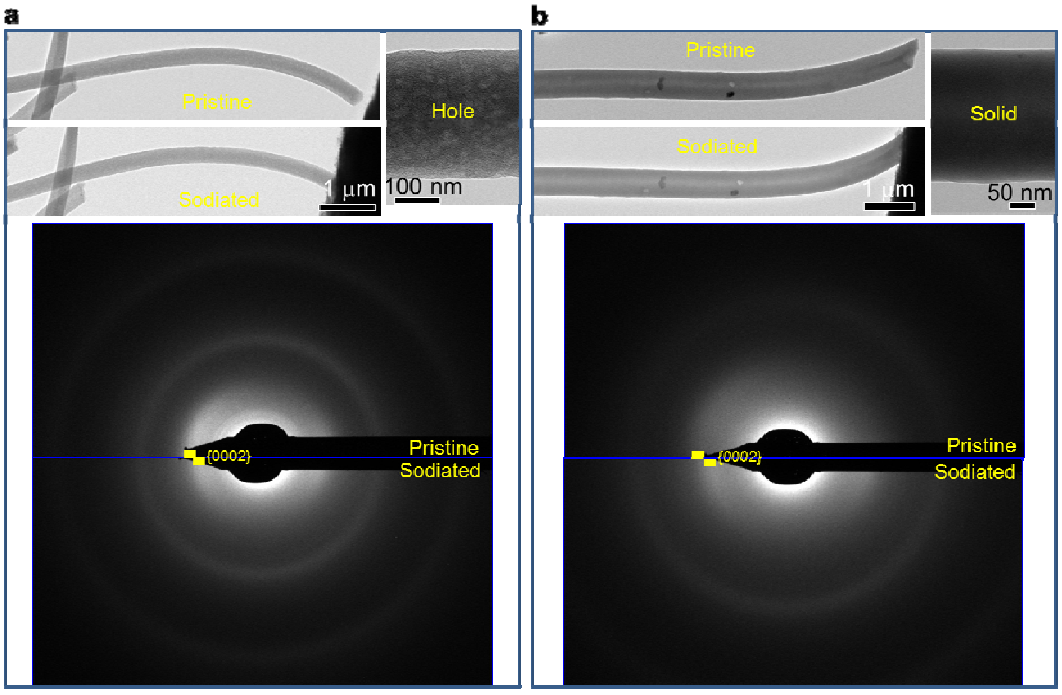


**Figure 3.16** Microstructure evolution of monolithic *d*-C CNFs with solid (a) or hollow (b) structures. No cracking is observed during the sodiation of these monolithic *d*-C CNFs. EDP confirms that the CNFs are sodiated.

### 3.5.3 Chemo-mechanical modeling of sodiation-induced stress and crack

To understand the observed interface cracking in CNFs, it is essential to elucidate the mechanism of stress generation during sodiation (and potassiation). Specifically, one needs to explain the origin of a large radial tensile stress driving the interface crack formation in hollow bilayer CNFs, as schematically shown in Figure 3.17.

To this end, we develop a continuum chemo-mechanical model to simulate the concurrent processes of Na diffusion and mechanical deformation. In the model, the

strain at any material point $\varepsilon_{ij}$ is assumed to consist of two parts, $\varepsilon_{ij} = \varepsilon_{ij}^{c} + \varepsilon_{ij}^{m}$, where $\varepsilon_{ij}^{c}$ is the chemical strain induced by Na insertion under a stress-free condition and $\varepsilon_{ij}^{m}$ is the elastic strain due to chemically-induced mechanical deformation. The components of chemical strain $\varepsilon_{ij}^{c}$ depend on the underlying atomic processes of Na insertion in *c*-C and *d*-C. And a physical assignment of the appropriate values for $\varepsilon_{ij}^{c}$ is critical to explain the stress generation and associated cracking response.

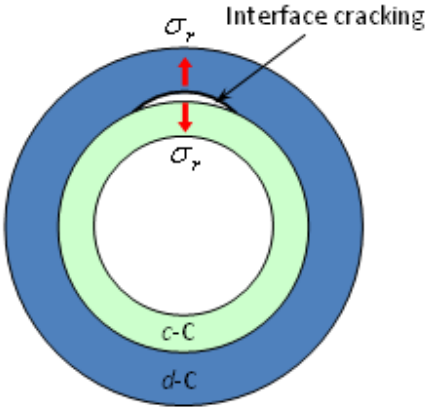


**Figure 3.17** Schematic of crack formation at the *c*-C/*d*-C interface, which is caused by a large radial tensile stress $\sigma_r$ at the interface.

We note that *c*-C consists of parallel graphene layers, and interlayer expansion is the primary deformation mode upon Na insertion. Hence, we assume the chemical strain $\varepsilon_{ij}^{c}$ is highly anisotropic with only one non-zero component perpendicular to graphene layers, i.e., in the radial direction of a CNF. In contrast, *d*-C consists of patches of few-layered graphene that are approximately aligned in the radial direction of a CNF. As a result, Na insertion in *d*-C would occur within the graphene layers, as well as in the open space among few-layered graphene patches[77]. Hence the chemical strain $\varepsilon_{ij}^{c}$ in *d*-C is likely less anisotropic than that in *c*-C. In addition, as the

longitudinal elongation of the CNFs is negligibly small, the plane strain condition is assumed.

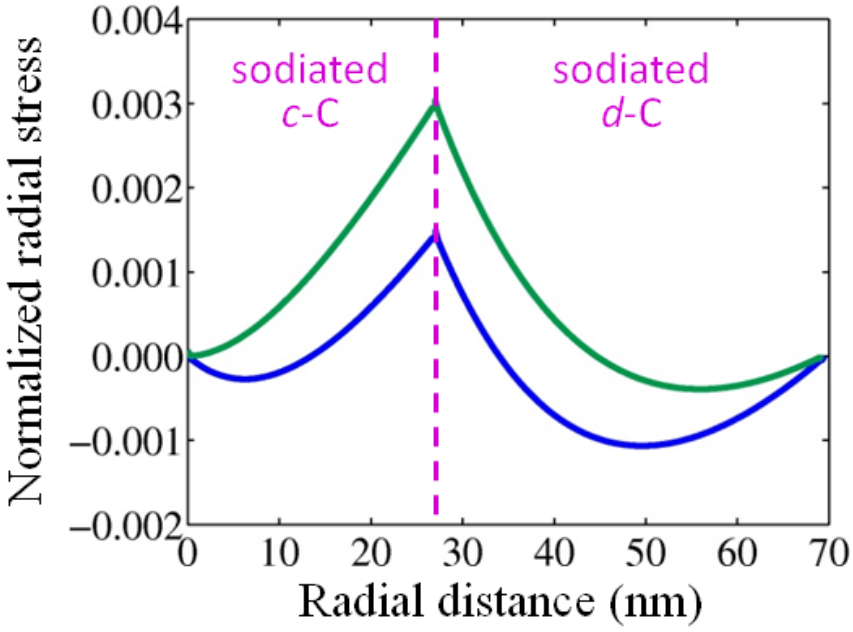


**Figure 3.18** Normalized radial stress ($\sigma_r/E$) versus radial distance $r$, being zero at the inner wall of the bilayer tube. The blue line corresponds to $\varepsilon_r^{c,d-C}=0.12,\ \varepsilon_\theta^{c,d-C}=\varepsilon_z^{c,d-C}=0.029$, while the green line corresponds to $\varepsilon_r^{c,d-C}=0.11,\ \varepsilon_\theta^{c,d-C}=\varepsilon_z^{c,d-C}=0.034$.

Finite element simulations based on the above chemo-mechanical model predict a radial tensile stress near the *c*-C/*d*-C interface which could be responsible for the interface cracking in sodiated bilayer CNFs (Figure 3.17). Based on the experimental data of volumetric chemical strains (being 6.0% and 18.7% in *c*-C and *d*-C layers, respectively) and considering the anisotropic nature of chemical strains as discussed above, we take $\varepsilon_r^{c,c-C}=0.06,\ \varepsilon_\theta^{c,c-C}=\varepsilon_z^{c,c-C}=0$ for *c*-C, and

$\varepsilon_r^{c,d-C} = 0.12,\ \varepsilon_\theta^{c,d-C} = \varepsilon_z^{c,d-C} = 0.029$ for *d*-C.

The blue line in Figure 3.18 shows the corresponding distribution of the radial stress $\sigma_r$, normalized by Young's modulus $E$. $\sigma_r$ is tensile and it reaches the maximum at the *c*-C/*d*-C interface, therefore providing a driving force of interface cracking. It should be noted that previous studies have emphasized the critical role of the chemical-strain anisotropy in stress generation[78-80]. In the present hollow bilayer CNFs, reducing the degree of anisotropy of the chemical strain in *d*-C is key to producing a large tensile radial stress near the *c*-C/*d*-C interface.

In Figure 3.18, the green line shows the $\sigma_r$ distribution for a different combination of chemical strains in the *d*-C layer ($\varepsilon_r^{c,d-C} = 0.11,\ \varepsilon_\theta^{c,d-C} = \varepsilon_z^{c,d-C} = 0.034$), while keeping the volumetric chemical strain constant. As the chemical strain becomes more isotropic, the interface tensile stress increases so as to facilitate the crack formation. At the moment of this study, the components of chemical strains cannot be directly measured, since the in situ TEM setup is incapable of measuring the mechanical properties of nano-sized electrodes.

### 3.5.4 Structure change of amorphous silicon-coated CNF during sodiation

To further understand the coupling between mechanical and electrochemical responses in CNFs, the sodiation behavior of an *a*-Si coated CNF (*a*-Si/CNF) is also investigated, see Figure 3.19 and Figure 3.20. The *a*-Si layer is coated on the outer surface of the CNF with a thickness of ~ 19 nm (Figure 3.19a,d). Due to geometrical confinement of the stiff *a*-Si coating, the sodiated bilayer tends to expand inward to the hollow space of CNF, resulting in a large decrease of the inner tube diameter.

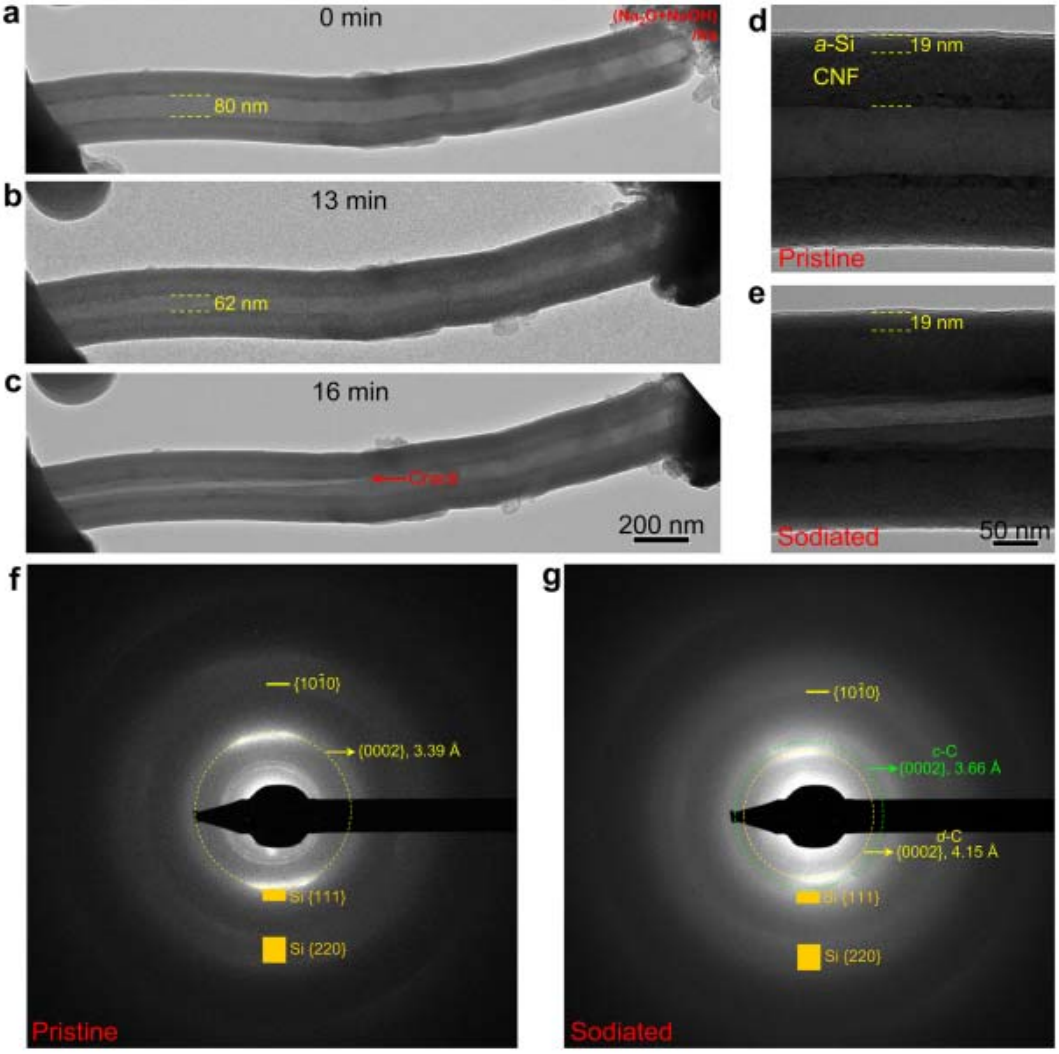


**Figure 3.19** (a, d) A pristine CNF with *a*-Si coating (~19 nm in thickness). The diameter of the inner wall is about 80 nm. (b) Upon sodiation, the diameter of the inner wall decrease to ~ 62 nm at the moment of crack formation. (c, e) The crack finally forms along the longitudinal direction of the *a*-Si/CNF system. The thickness of the *a*-Si coating does not change after sodiation, indicating no reaction occurs. (f-g) EDPs of the pristine and sodiated *a*-Si/CNF. The sodiated CNF exhibits a typical split EDP, while no change is observed in the diffraction rings of *a*-Si before and after sodiation, confirming no reaction occurs in *a*-Si.

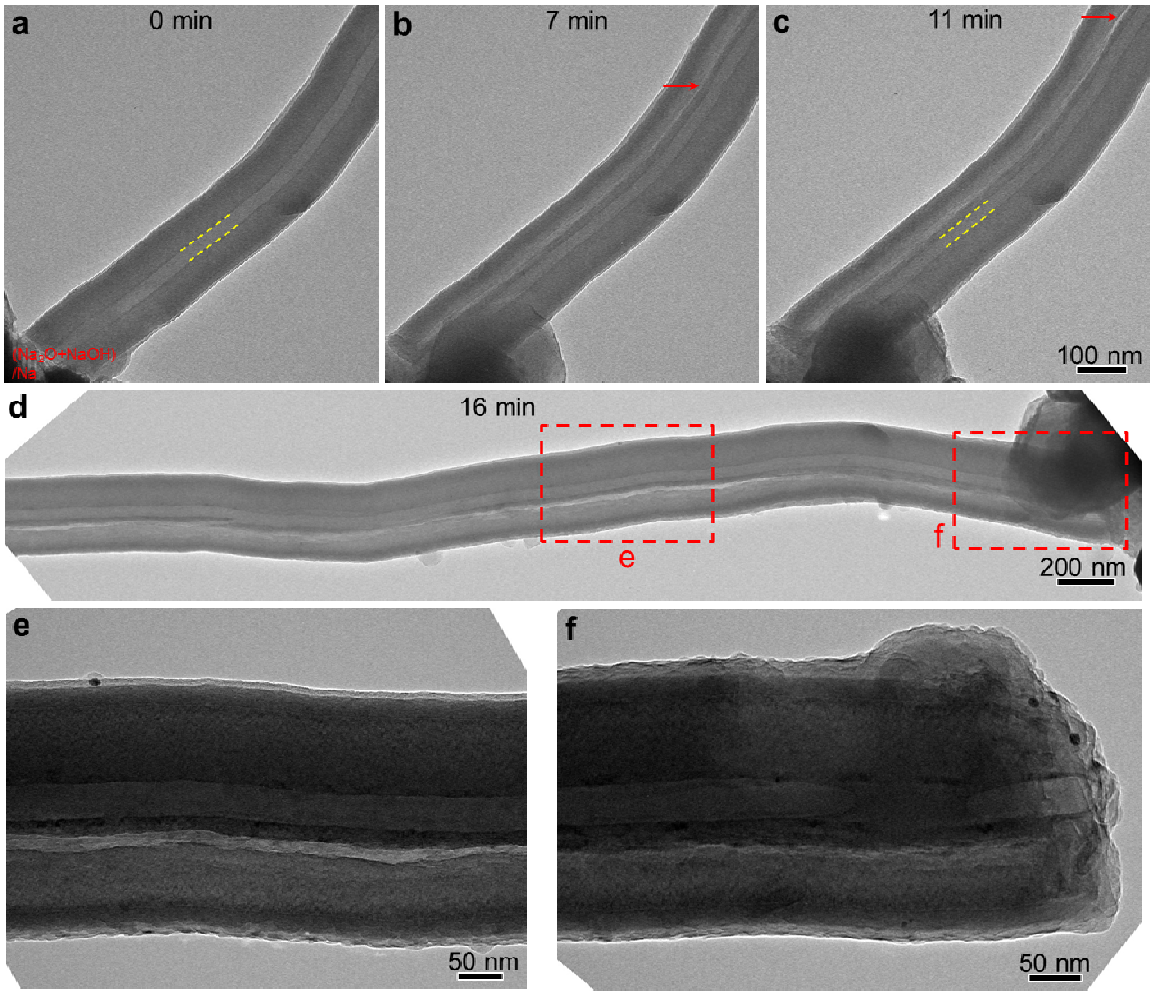


**Figure 3.20** Microstructure evolution of an amorphous silicon-coated CNF (*a*-Si/CNF) before and after sodiation. (a-d) Sequential images showing the crack nucleation and growth upon sodiation, accompanied with the decrease of the inner tube diameter. (e-f) Zoom-in images showing the cracks the interface between *c*-C and *d*-C. The thickness of the surface *a*-Si layer does not change after sodiation, indicating no reaction occurring.

Upon sodiation, the diameter of the inner wall gradually reduces due to the geometric confinement of the stiff *a*-Si coating, and it decrease to ~ 62 nm at the moment of crack formation. Similar to the case without coating, sodiation also leads

to crack formation along the longitudinal direction of the *a*-Si/CNF (Figure 3.19c), and cracking occurs near the *c*-C/*d*-C interface (Figure 3.20).

Note that the thickness of the *a*-Si coating remains unchanged during sodiation, indicating negligible Na insertion in *a*-Si. This is further confirmed by EDPs of the *a*-Si/CNF before and after sodiation (Figure 3.19f-g). The sodiated CNF shows a typical split EDP, while no change is observed in the diffraction rings of *a*-Si before and after sodiation. These in situ TEM results suggest that nanoscale *a*-Si may not be a viable anode material for NIBs. A previous theoretical study indicates that Si may serve as an anode material for NIBs[8], despite the lack of direct experimental support to date[15]. Our in situ TEM study indicates that *a*-Si is electrochemically unfavorable for NIBs. Moreover, the surface coating of *d*-C or amorphous C has been widely used to enhance the electronic conductivity or serve as a supporting material for nanocomposite electrodes of NIBs[50-52]. The present sodiation study of *a*-Si/CNF also suggests that even when *d*-C is covered with an inactive surface layer, it can still be effectively sodiated or potassiated, likely due to the fast diffusion of Na and K ions at the interface.

### *3.6 Summary*

In summary, carbonaceous materials have great potential for applications as anodes of alkali-metal ion batteries, such as Na-ion batteries and K-ion batteries (NIB and KIBs). We conduct an *in situ* study of the electrochemically-driven sodiation and potassiation of individual carbon nanofibers (CNFs) by transmission electron microscopy (TEM). The CNFs are hollow and consist of a bilayer wall with an outer layer of disordered-carbon (*d*-C) enclosing an inner layer of crystalline-carbon (*c*-C).

The *d*-C exhibits about three times volume expansion of the *c*-C after full sodiation or potassiation, thus suggesting a much higher storage capacity of Na or K ions in *d*-C than *c*-C. For the bilayer CNF-based electrode, a steady capacity of 245 mAh/g is measured with a Coulombic efficiency approaching 98% after a few initial cycles. Our in situ TEM experiments also reveal the mechanical degradation of CNFs through formation of longitudinal cracks near the *c*-C/*d*-C interface during sodiation and potassiation. Such cracking behavior is attributed to the generation of a large radial tensile stress near the *c*-C/*d*-C interface, which arises due to the different sodiation/potassiation strains in *c*-C and *d*-C. Our results provide mechanistic insights into the electrochemical reaction, microstructure evolution and mechanical degradation of carbon-based anodes during sodiation and potassiation, shedding light onto the development of carbon-based electrodes for NIBs and KIBs.

# Chapter 4: Conclusion and future work

## *4.1 Conclusion*

Carbon materials are often used to enhance the electronic conductivity in anodes or cathodes of Li-ion batteries (LIBs), as well as to support other active materials in high-capacity nanocomposite electrodes. In the first work, a novel tellurium/porous carbon (Te/C) composite is synthesized at a high temperature of 600 $^{o}$C under vacuum. The designed Te/C composite is employed, for the first time, as cathode material in lithium-ion batteries, which exhibits excellent electrochemical performance in commercialized carbonate-based electrolyte. Owing to the physical confinement and chemical stabilization of tellurium in the supporting carbon matrix, the Te/C electrode can deliver a reversible volumetric capacity of 1400 mAh/cm$^3$ (224 mAh/g) and a high Coulombic efficiency near 99% over up to 1000 cycles without any further capacity decay. The high volumetric capacity, long cycle life, excellent Coulombic efficiency and good rate capability of Te/C composite demonstrates that Li-Te batteries are promising candidates for applications in large-scale and high-energy storage.

In the second work, we conduct an *in situ* study of the electrochemically-driven sodiation and potassiation of individual carbon nanofibers (CNFs) by transmission electron microscopy (TEM). The CNFs are hollow and consist of a bilayer wall with an outer layer of disordered-carbon (*d*-C) enclosing an inner layer of crystalline-carbon (*c*-C). The *d*-C exhibits about three times volume expansion of the *c*-C after full sodiation/potassiation, thus suggesting a much higher storage capacity

of Na/K ions in *d*-C than *c*-C. For the bilayer CNF-based electrode, a steady capacity of 245 mAh/g is measured with a Coulombic efficiency approaching 98% after a few initial cycles. Our in situ TEM experiments also reveal the mechanical degradation of CNFs through formation of longitudinal cracks near the *c*-C/*d*-C interface during sodiation/potassiation. Such cracking behavior is attributed to the generation of a large radial tensile stress near the *c*-C/*d*-C interface, which arises due to the different strains in *c*-C and *d*-C. Our results provide mechanistic insights into the electrochemical reaction, microstructure evolution and mechanical degradation of carbon-based anodes during sodiation and potassiation, shedding light onto the development of carbon-based electrodes for NIBs and KIBs.

### *4.2 Future work*

Although the lithium-tellurium batteries based on Te/porous carbon cathode has obtained excellent cycling stability, ratability and Coulombic efficiency, it is still far away from commercialization due to capacity decay in the first few cycles. The most simple and practical part of future work can be targeted onto improving the capacity of Te/porous carbon composite using high surface area porous carbon or forming chemical bonding between Te and carbon to further stabilize the Te except the physical confinement.

In addition, although the in situ technology enables us to investigate the morphology and structure change of CNFs during sodiation/potassiation, the solid cell inside of TEM is different from liquid cell using organic electrolyte. Thus more advanced nano-batteries inside TEM need to be created to allow the application of

liquid electrolyte in TEM. Moreover, despite the excellent cycle life of CNFs anode in NIBs, the cycling stability of CNFs electrode for K-ion battery is still not good, probably due to the kinetics problems of larger K ions, thus other CNFs, like highly-disordered carbon, might be a way for a better cycling stability for KIBs, since highly-disordered carbon possesses more defects than lower-disordered carbon, which can provide more sites for potassium insertion.

# Bibliography


1. J.M. Tarascon, M. Armand, *Nature*. 2001, 414, 359.
2. K.S. Kang, Y.S. Meng, J. Breger, C.P. Grey, G. Ceder, *Science*. 2006, 311, 977.
3. H. Wu, G. Yu, L. Pan, N. Liu, M.T. McDowell, Z. Bao, Y. Cui, *Nat. Commun.* 2013, 4, 1943.
4. C.K. Chan, H. Peng, G. Liu, K. McIlwrath, X.F. Zhang, R.A. Huggins, Y. Cui, *Nat. Nanotechnol*. 2008, 3, 31.
5. Y. Liu, Y. Xu, Y. Zhu, J.N. Culver, C.A. Lundgren, K. Xu, C. Wang, *ACS Nano.* 2013, 7, 3627.
6. L.W. Ji, Z. Lin, M. Alcoutlabi, X.W. Zhang, *Energy Environ. Sci.* 2011, 4, 2682.
7. Y.S. Jang, Y.C. Kang, *Phys. Chem. Chem. Phys.* 2013, 15, 16437.
8. S-B. Son, T.A. Yersak, D.M. Piper, S.C. Kim, C.S. Kang, J.S. Cho, S-S Suh, Y-U. Kim, K.H. Oh, S-H. Lee, *Adv. Energy. Mater.* 2013, DOI: 10.1002/aenm.201300961.
9. J-M Jeong, B.G. Choi, S.C. Lee, K.G. Lee, S-J Chang, Y-K Han, Y.B. Lee, H.U. Lee, S.Kwon, G. Lee, C-S Lee, YS. Huh, *Adv. Mater.* 2013, 25, 6250.
10. M.D. Slater, D. Kim, E. Lee, C.S Johnson, *Adv. Funct. Mater.* 2013, 23, 947.
11. K. Tang, L. Fu, R.J. White, L. Yu, M.M Titirici, M. Antonietti, J. Maier, *Adv. Energy Mater.* 2012, 2, 873.
12. C.D.Wessells, S.V. Peddada, R.A. Huggins, Y. Cui, *Nano Lett.* 2011, 11, 5421.
13. K.T. Lee, S.Y. Hong, Y. Kim, Y. won Park, A.Choi, N.S. Choi, *Energy Environ. Sci.* 2013, 6, 2067.

14. V. Palomares, M. Casas-Cabanas, E. Castillo-Martinez, M.H. Han, T. Rojo, *Energy Environ. Sci.* 2013, 6, 2312.

15. V. Etacheri, R. Marom, R. Elazari, G. Salitra, D. Aurbach, *Energy Environ. Sci.,* 2011, 4, 3243.

16. T.H. Kim, J.S. Park, S.K. Chang, S. Choi, J.H. Ryu, H.K. Song, *Adv. Energy. Mater.,* 2012, 2, 860.

17. M.M. Shaijumon, E. Perre, B. Daffos, P.L. Taberna, J.M. Tarascon, P. Simon *Adv. Mater.*, 2010, 22, 4978.

18. X. Chen, K. Gerasopoulos, J. Guo, A. Brown, C. Wang, C. *ACS Nano*, 2010, 4, 366.

19. V.P. Phan, B. Pecquenard, F.L. Cras, *Adv. Funct. Mater.*, 2012, 22, 2580.

20. Y.J. Lee, A.M. Belcher, *J. Mater. Chem.*, 2011, 21, 1033.

21. P.G. Bruce, S.A. Freunberger, L.J. Hardwick, J-M. Tarascon, *Nat. Mater.* 2012, 11, 19.

22. J. Guo, Y. Xu, C. Wang, *Nano Lett.* 2011, 11 4288.

23. Z.W. She, W. Li, J.J. Cha, G. Zheng, Y. Yang, M.T. McDowell, P-C. Hsu, Y. Cui, *Nat. Commun.* 2013, 4, 1331.

24. H. Wang, Y. Yang, Y. Liang, J.T. Robinson, Y. Li, A. Jackson, Y. Cui, H. Dai, *Nano Lett,* 2011, 11, 2644.

25. X. Ji, K.T. Lee, L.F. Nazar, *Nat. Mater.* 2009, 8, 500.

26. J. Schuster, G. He, B.Mandlmeier, T. Yim, K.T. Lee, T. Bein, L.F. Nazar, *Angew. Chem. Int. Ed.* 2012, 51, 3591.

27. J. Wang, J. Yang, J. Xie, N. Xu, *Adv. Mater.* 2002, 14, 963.

28. L. Xiao, Y. Cao, J. Xiao, B. Schwenzer, M.H. Engelhard, L.V. Saraf, Z. Nie, G.J. Exarhos, J. Liu, *Adv. Mater.* 2012, 24, 1176.

29. E.S. Shin, K. Kim, S.H. Oh, W.I. Cho, *Chem. Commun.* 2013, 49, 2004.

30. A. Abouimrane, D. Dambournet, K.W. Chapman, P.J. Chupas, W. Weng, K. Amine, *J. Am. Chem. Soc.* 2012, 134, 4505.

31. C-P. Yang, S. Xin, Y-X. Yin, H. Ye, J. Zhang, Y-G. Guo, *Angew. Chem. Int. Ed.* 2013, 52, 1.

32. C. Luo, Y. Xu, Y. Zhu, Y. Liu, S. Zheng, Y. Liu, A. Langrock, C. Wang, *ACS Nano.* 2013, 7, 8003.

33. H.S. Kim, T.S. Arthur, G.D. Allred, J. Zajicek, J.G. Newman, A.E. Rodnyansky, A.G. Oliver, W.C. Boggess, J.Muldoon, *Nat. Commun.* 2011, 2, 427.

34. V.L. Chevrier, G. Ceder, *J. Electrochem. Soc.* 2011, 158, A1011.

35. L.D. Ellis, T.D. Hatchard, M.N. Obrovac, *J. Electrochem. Soc.* 2012, 159, A1801.

36. J.W. Wang, X.H. Liu, S.X Mao, J.Y. Huang, *Nano Lett.* 2012, 12, 5897.

37. H. Xiong, M.D. Slater, M. Balasubramanian, C.S. Johnson, T. Rajh, *J. Phys. Chem. Lett.* 2011, 2, 2560.

38. Y. Cao, L. Xiao, W. Wang, D. Choi, Z. Nie, J. Yu, L.V. Saraf, Z. Yang, J. Liu, *Adv. Mater.* 2011, 23, 3155.

39. R. Alcántara, J.M. Jiménez-Mateos, P. Lavela, J.L. Tirado, *Electrochem. Commun.* 2001, 3, 639.

40. R. Alcántara, P. Lavela, G.F. Ortiz, J.L. Tirado, *Electrochem. Solid-State Lett.* 2005, 8, A222.

41. Y. Cao, L. Xiao, M.L. Sushko, W. Wang, B. Schwenzer, J. Xiao, Z. Nie, L.V.

Saraf, Z. Yang, J. Liu, J. *Nano Lett.* 2012, 12, 3783.

42. S. Komaba, W. Murata, T. Ishikawa, N. Yabuuchi, T. Ozeki, T. Nakayama, A. Ogata, K. Gotoh, K. Fujiwara, *Adv. Funct. Mater.* 2011, 21, 3859.
43. S. Wenzel, T. Hara, J. Janek, P. Adelhelm, *Energy Environ. Sci.* 2011, 4, 3342.
44. J. Zhao, L. Zhao, K. Chihara, S. Okada, J. Yamaki, S. Matsumoto, S. Kuze, K. Nakane, *J. Power Sources* 201), 244, 752.
45. D. Stevens, J. Dahn, *J. Electrochem. Soc.* 2000, 147, 1271
46. B. Scrosati, *Electrochim. Acta* 2000, 45, 2461.
47. D. Stevens, J. Dahn, *J. Electrochem. Soc.* 2001, 148, A803.
48. Y. Shao, J. Xiao, W. Wang, M. Engelhard, X. Chen, Z. Nie, M. Gu, L. Saraf, G. Exarhos, J. Zhang, J. Liu, *Nano Lett.* 2013, 13, 3909.
49. Y. Kim, Y. Park, A. Choi, N. Choi, J. Kim, J. Lee, J.H. Ryu, S. Oh, K.T. Lee, *Adv. Mater.* 2013, 25, 3045.
50. J. Qian, Y. Chen, L. Wu, Y. Cao, X. Ai, H.Yang, *Chem. Commun.* 2012, 48, 7070.
51. L. Xiao, Y. Cao, J. Xiao, W. Wang, L. Kovarik, Z. Nie, J. Liu, J. *Chem. Commun.* 2012, 48, 3321.
52. Y. Zhu, X. Han, Y. Xu, Y. Liu, S. Zheng, K Xu, L. Hu, C. Wang, C. *ACS Nano* 2013, 7, 6378.
53. Y. Zhu, J.W. Wang, Y. Liu, X. Liu, A. Kushima, Y. Liu, Y. Xu, S.X. Mao, J. Li, C. Wang, J.Y. Huang, *Adv. Mater.* 2013, 25, 5461.
54. J.W. Wang, Y. He, F. Fan, X.H. Liu, S. Xia, Y. Liu, C.T. Harris, H. Li, J.Y. Huang, S.X. Mao, *Nano Lett.* 2013, 13, 709.

55. J.W. Wang, X.H. Liu, K. Zhao, A. Palmer, E. Patten, D. Burton, S.X. Mao, Z. Suo, J.Y. Huang, *ACS Nano* 2012, 6, 9158.

56. X. Liu, J.Y. Huang. Energy Environ. Sci (2011), 4, 3844.

57. Q.Q Xiong, Y. Lu, X.L. Wang, C.D. Gu, Y.Q. Qiao, J.P. Tu, *J. Alloys Compd.* 2012, 536, 219.

58. M. Armand, J.M. Tarascon, *Nature.* 2008, 451, 652.

59. J.W. Wang, X.H. Liu, K. Zhao, A. Palmer, E. Patten, D. Burton, S.X. Mao, Z. Suo, J.Y. Huang, *ACS nano.* 2012, 6, 9158.

60. J.B. Goodenough, Y. Kim, *Chem. Mater.* 2010, 22, 587.

61. S.A. Webb, L. Baggetto, C.A. Bridges, G.M. Veith, *J. Power Sources*. 2014, 248, 1105.

62. Y. Xu, Y. Zhu, Y. Liu, C. Wang, *Adv. Energy. Mater.*2013, 3, 128.

63. P. Meduri, C. Pendyala, V. Kumar, G.U. Sumanasekera, M.K. Sunkara, *Nano Lett.* 2009, 9, 612.

64. T. Ramireddy, M.M. Rahman, T. Xing, Y. Chen, A.M. Glushenkov, *J. Mater. Chem. A.* 2014, 2, 4282.

65. C.B. Bucur, J. Muldoon, A. Lita, J. B. Schlenoff, R.A. Ghostine, S. Dietz, G. Allred, *Energy Environ. Sci.* 2013, 6, 3286.

66. H. Kim, J.T. Lee, D.C. Lee, A. Magasinski, W. Cho, G. Yushin, *Adv. Energy. Mater.* 2013, 3, 1308.

67. H.T. Kwon, C.M. Park, *J. Power Sources*. 2014, 251, 319.

68. V.V. Poborchii, *Solid State Commun.* 1998, 107, 513.

69. J-M. Song, Y-Z Lin, Y-J. Zhan, Y-C. Tian, G Liu, S-H Yu, *Cryst. Growth Des.*

2008, 8, 1902.

70. C.K. Chan, H. Peng, G. Liu, K. McIlwrath, X.F. Zhang, R.A. Huggins, Y. Cui, *Nat. Nanotechnol.* 2008, 3, 31.
71. V. Etacheri, R. Marom, R. Elazari, G. Salitra, D. Aurbach, *Energy Environ. Sci.* 2011, 4, 3243.
72. A. Eftekhari. J. Power Sources. 2004, 126, 221.
73. X. Zhou, Y. Guo, *ChemElectroChem* 2014, 1, 83.
74. Y. Liu, H. Zheng, X.H. Liu, S. Huang, T. Zhu, J. Wang, A. Kushima, N.S. Hudak, X. Huang, S. Zhang, S.X. Mao, X. Qian, J. Li, J.Y. Huang, *ACS Nano* 2011, 5, 7245.
75. X.H. Liu, J.W. Wang, Y. Liu, H. Zheng, A. Kushima, S. Huang, T. Zhu, S.X. Mao, J. Li, S. Zhang, W. Lu, J.M. Tour, J.Y. Huang, *Carbon* 2012, 50, 3836.
76. X.H. Liu, Y. Liu, A. Kushima, S. Zhang, T. Zhu, J. Li, J.Y. Huang, *Advanced Energy Materials* 2012, 2, 722.
77. P. Thomas, D. Billaud, *Electrochim. Acta* 2001, 46, 3359.
78. C.H. Hsueh, A.G. Evans, *Journal of Applied Physics.* 1983, 54, 6672.
79. S. Huang, F. Fan, J. Li, S., Zhang, T. Zhu, *Acta Materialia.* 2013, 61, 4354.
80. W. Liang, H. Yang, F. Fan, Y. Liu, X.H. Liu, J.Y. Huang, T. Zhu, S. Zhang, *ACS Nano* 2013, 7, 3427.

# Publication and Presentation

*Publication*

1. **Y. Liu**, J. Wang, Y. Zhu, Y. Xu, D. Bigio, C. Wang, "Lithium-tellurium batteries based on tellurium/porous carbon composite", *J. Mater. Chem. A*, 2014, DOI: 10.1039/C4TA02075H

2. **Y. Liu**, F. Fan, J. Wang, Y. Liu, H. Chen, K.L. Jungjohann, Y. Xu, Y. Zhu, D. Bigio, T. Zhu, C. Wang, "In situ Transmission Electron Microscopy Study of Electrochemical Sodiation and Potassiation of Carbon Nanofibers", *Nano Letter*, 2014, 14, 3445

3. C. Luo, Y, Xu, Y. Zhu, Y. Liu, S Zheng, **Y. Liu**, A. Langrock, C. Wang, "Selenium@Mesoporous Carbon Composite with Superior Lithium and Sodium Storage Capacity", *ACS Nano*, 2013, 7, 8003

*Presentation*

**Y. Liu**, G. Rosen, D, Bigio and C. Wang, "A new rechargeable Li-ion battery using dendrimer-nitroxide as cathode material through Li-ion adsorption/desorption mechanism", 224$^{th}$ ECS meeting, San Francisco, Nov. 2013.